

# Unraveling the Scotogenic Model at Muon Collider

---

Jiao Liu<sup>1,2</sup>, Zhi-Long Han<sup>1</sup>, Yi Jin<sup>1,2</sup>, Honglei Li<sup>1</sup>

<sup>1</sup>*School of Physics and Technology, University of Jinan, Jinan, Shandong, 250022, China*

<sup>2</sup>*Guangxi Key Laboratory of Nuclear Physics and Nuclear Technology, Guangxi Normal University, Guilin, Guangxi 541004, China*

*E-mail:* [sps\\_hanzl@ujn.edu.cn](mailto:sps_hanzl@ujn.edu.cn), [ss\\_jiny@ujn.edu.cn](mailto:ss_jiny@ujn.edu.cn)

**ABSTRACT:** The Scotogenic model extends the standard model with three singlet fermion  $N_i$  and one inert doublet scalar  $\eta$  to address the common origin of tiny neutrino mass and dark matter. For fermion dark matter  $N_1$ , a hierarchical Yukawa structure  $|y_{1e}| \ll |y_{1\mu}| \sim |y_{1\tau}| \sim \mathcal{O}(1)$  is usually favored to satisfy constraints from lepton flavor violation and relic density. Such large  $\mu$ -related Yukawa coupling would greatly enhance the pair production of charged scalar  $\eta^\pm$  at the muon collider. In this paper, we investigate the dilepton and mono-photon signature of the Scotogenic model at a 14 TeV muon collider. For the dimuon signature  $\mu^+\mu^- + \cancel{E}_T$ , we find that most viable samples can be probed with  $200 \text{ fb}^{-1}$  data. The ditau signature  $\tau^+\tau^- + \cancel{E}_T$  is usually less promising, but it is important to probe the small  $|y_{1\mu}|$  region. The mono-photon signature  $\gamma + \cancel{E}_T$  could also probe the compressed mass region  $M_1 \lesssim M_{\eta^\pm}$ . Masses of charged scalar  $\eta^\pm$  and dark matter  $N_1$  can be further extracted by a binned likelihood fit of the dilepton energy.

---

## Contents

<b>1</b>	<b>Introduction</b>	<b>1</b>
<b>2</b>	<b>The Scotogenic Model</b>	<b>3</b>
<b>3</b>	<b>Lepton Flavor Violation</b>	<b>5</b>
<b>4</b>	<b>Dark Matter</b>	<b>6</b>
<b>5</b>	<b>Signatures at Muon Collider</b>	<b>10</b>
5.1	$\mu^+\mu^- + \cancel{E}_T$ Signature	12
5.2	$\tau^+\tau^- + \cancel{E}_T$ Signature	17
5.3	Mono- $\gamma$ Signature	20
5.4	Mass Measurement	23
<b>6</b>	<b>Conclusion</b>	<b>26</b>

---

## 1 Introduction

There are solid astrophysical and cosmological observations that indicate the existence of dark matter. Meanwhile, the neutrino oscillation experiments have confirmed that neutrinos have nonzero but tiny masses. To explain the origin of dark matter and tiny neutrino masses, we need to seek new physics beyond the standard model. Among various theoretical models to address them, the most appealing pathway is interpreting these two issues within the same framework [1–8].

The Scotogenic model [3] is an attractive option, where dark matter acts as the messenger of neutrino mass at the one-loop level. To realize this, an exact  $Z_2$  symmetry is imposed, which forbids the tree-level neutrino mass and also stabilizes the dark matter. This model further introduces three singlet fermions  $N_i$  and one inert scalar doublet  $\eta$ . The new particles are odd under the  $Z_2$  symmetry. Phenomenological studies of the Scotogenic model have been extensively performed in Refs. [9–23]. In principle, either the lightest neutral scalar or the lightest fermion can serve as the dark matter candidate. For the scalar dark matter scenario, quite a large portion of the parameter space with correct relic density can be probed via direct detection [24–26], indirect detection [27–29], and collider experiments [30–34]. For instance, the low-mass regime with dark matter mass in the range of  $55 \sim 75$  GeV can be tested in direct detection experiments [25]. Meanwhile, the high-mass regime with dark matter mass above 500 GeV is mostly within the reach of the Cherenkov Telescope Array [27, 28].

As for the fermion dark matter scenario, the dark matter-nucleon scattering appears at the one-loop level [13, 35]. Therefore, the corresponding cross-section is naturally suppressed by the loop factor. However, under certain circumstances, such as the two singlet fermions  $N_1$  and  $N_2$  nearly degenerating [13] or sufficiently large quartic couplings between inert scalar and Standard Model Higgs [35], we still have the chance to probe at upcoming direct detection experiments. On the other hand, the annihilation cross-section of fermion dark matter at present time is  $p$ -wave suppressed, due to the Majorana nature of  $N_1$  [9]. In this way, the indirect detection experiments are hard to have positive signals.

One appealing way to probe the fermion dark matter is via the lepton flavor violating processes [36]. The future sensitivities of corresponding observables could exclude dark matter mass below 100 GeV [37]. Another promising pathway is the dilepton signatures with missing transverse energy  $\cancel{E}_T$  at colliders [38]. This signature arises from the pair production of the charged scalar  $\eta^\pm$  at colliders with the cascade decay  $\eta^\pm \rightarrow \ell^\pm N_1$ . Searches for similar signatures have been performed in the framework of supersymmetry at LHC [39–41]. Currently, the 13 TeV LHC has excluded the region with  $M_{\eta^\pm} \lesssim 700$  GeV and  $M_N \lesssim 400$  GeV. For future colliders, the 3 TeV CLIC and the 100 TeV FCC-hh could probe  $M_{\eta^\pm} \lesssim 1500$  GeV and  $M_N \lesssim 2000$  GeV, respectively [38].

The multi-TeV muon collider has received growing interest in recent years [42–60]. It is an ideal machine to probe potential new physics correlated with muon, e.g.,  $(g-2)_\mu$  [61–66] and  $R_K$  anomaly [67–71]. Under the tight constrain from  $\mu \rightarrow e\gamma$ , the new Yukawa couplings of the Scotogenic model have a hierarchical structure as  $|y_{1e}| \ll |y_{1\mu}| \lesssim |y_{1\tau}| \sim \mathcal{O}(1)$  [37]. Therefore, pair production of charged scalar at muon collider could be greatly enhanced due to additional contribution from the  $t$ -channel exchange of  $N_i$  with relatively large Yukawa coupling  $|y_{i\mu}| \sim \mathcal{O}(1)$ . Then, the muon collider is more competitive than the  $e^+e^-$  and  $pp$  colliders in searching for the Scotogenic model.

In this paper, we investigate the dilepton signature of the Scotogenic model at a multi-TeV muon collider (MuC). According to our scan of the parameter space in Section 4, the charged scalar mass could be up to about 6 TeV with the Yukawa coupling  $|y_{i\alpha}| \lesssim 3$ . In order to fully access the charged scalar, we take the benchmark choice of the collider energy and the corresponding final integrated luminosity as  $\sqrt{s} = 14$  TeV with  $\mathcal{L} = 20 \text{ ab}^{-1}$  [45]. As will be shown later, a 14 TeV muon collider can easily cover a significant part of the parameter space of fermion dark matter. Furthermore, the mass of charged scalar  $\eta^\pm$  and dark matter  $N_1$  are able to be extracted from the kinematic edges of the lepton energy distribution [72, 73].

The rest of the paper is organized as follows. In Section 2, we review the key structure of the Scotogenic model. Constraints from lepton flavor violating processes are discussed in Section 3. Phenomenology of dark matter is considered in Section 4. Viable parameter space is obtained under constraints from lepton flavor violation and relic density in this section. Dilepton signature, mono-photon signature and mass measurement at muon collider are studied in Section 5. The conclusion is in Section 6.

## 2 The Scotogenic Model

The Scotogenic model is originally proposed in Ref. [3] to explain the common origin of tiny neutrino mass and dark matter. This model has three singlet fermions  $N_i$  and one inert scalar doublet  $\eta$ , which are odd under a discrete  $Z_2$  symmetry. In this paper, we consider the lightest fermion  $N_1$  as the dark matter candidate and produced via the freeze-out mechanism. The scalar potential under the exact  $Z_2$  symmetry is

$$\mathcal{V} = m_\phi^2 \phi^\dagger \phi + m_\eta^2 \eta^\dagger \eta + \frac{\lambda_1}{2} (\phi^\dagger \phi)^2 + \frac{\lambda_2}{2} (\eta^\dagger \eta)^2 + \lambda_3 (\phi^\dagger \phi) (\eta^\dagger \eta) \quad (2.1)$$

$$+ \lambda_4 (\phi^\dagger \eta) (\eta^\dagger \phi) + \frac{\lambda_5}{2} [(\phi^\dagger \eta)^2 + (\eta^\dagger \phi)^2],$$

where  $m_\eta^2 > 0$  is required to avoid the broken of the  $Z_2$  symmetry [74]. Notably, the  $\lambda_5$ -term is the only source of lepton number violation, thus is naturally small. All the parameters in the scalar potential are taken to be real [75]. Constrained by the vacuum stability condition, the couplings in the scalar potential should satisfy [76]

$$\lambda_1 > 0, \lambda_2 > 0, \lambda_3 + \sqrt{\lambda_1 \lambda_2} > 0, \lambda_3 + \lambda_4 - |\lambda_5| + \sqrt{\lambda_1 \lambda_2} > 0. \quad (2.2)$$

After the electroweak symmetry breaking, masses of the Standard Model Higgs boson and inert scalars are

$$M_h^2 = \lambda_1 v^2, \quad (2.3)$$

$$M_{\eta^\pm}^2 = m_\eta^2 + \frac{1}{2} \lambda_3 v^2, \quad (2.4)$$

$$M_R^2 = m_\eta^2 + \frac{1}{2} (\lambda_3 + \lambda_4 + \lambda_5) v^2, \quad (2.5)$$

$$M_I^2 = m_\eta^2 + \frac{1}{2} (\lambda_3 + \lambda_4 - \lambda_5) v^2, \quad (2.6)$$

with  $M_R(M_I)$  denoting the mass of the real(imaginary) part of  $\eta^0$ . As discussed in Section 4, we fix  $\lambda_3 = \lambda_4 = 0.01$  to escape the tight constrain from dark matter direct detection. Meanwhile, the coupling  $\lambda_5$  is also very small to obtain tiny neutrino mass with sizable Yukawa coupling. Therefore, the mass spectrum of inert scalars are highly degenerate, i.e.,  $M_{\eta^\pm} \simeq M_R \simeq M_I$ . The contributions of inert scalars to the electroweak precision observables  $S$  and  $T$  are quite small with degenerate masses [77].

The new Yukawa interactions for neutrino masses generation are given by

$$- \mathcal{L}_Y \supset y_{i\alpha} \bar{N}_i \tilde{\eta}^\dagger L_\alpha + \frac{1}{2} M_i \bar{N}_i^c N_i + h.c., \quad (2.7)$$

where  $\tilde{\eta} = i\sigma_2 \eta^*$ . We also assume the mass matrix of singlet fermion  $M$  to be diagonal for simplicity. As shown in Figure 1, the neutrino mass is generated at one-loop level

$$m_\nu^{\alpha\beta} = \sum_{i=1}^3 \frac{y_{i\alpha} y_{i\beta}}{32\pi^2} M_i \left[ \frac{M_R^2}{M_R^2 - M_i^2} \log \left( \frac{M_R^2}{M_i^2} \right) - \frac{M_I^2}{M_I^2 - M_i^2} \log \left( \frac{M_I^2}{M_i^2} \right) \right] \quad (2.8)$$

$$\equiv \sum_{i=1}^3 y_{i\alpha} y_{i\beta} \Lambda_i \quad (2.9)$$

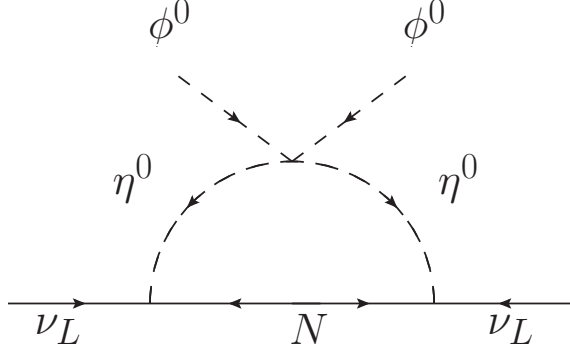


**Figure 1.** The one-loop neutrino mass generation in Scotogenic model.

Using the Casas-Ibarra parameterization [78], the Yukawa coupling  $y$  can be determined by the neutrino oscillation parameters

$$y = \sqrt{\Lambda}^{-1} R \sqrt{\hat{m}_\nu} U_{\text{PMNS}}^\dagger, \quad (2.10)$$

where  $\Lambda = \text{diag}(\Lambda_1, \Lambda_2, \Lambda_3)$ , and  $R$  is a complex orthogonal matrix. In this paper, we assume  $R$  is real for simplicity.  $\hat{m}_\nu = \text{diag}(m_1, m_2, m_3)$  is the diagonalized neutrino mass matrix.  $U_{\text{PMNS}}$  is the Pontecorvo-Maki-Nakagawa-Sakata (PMNS) matrix for neutrino mixing. In the following study, all the neutrino oscillation parameters are varied in the  $3\sigma$  range of the global fit result [79].

As will shown in Figure 2, sizable Yukawa coupling  $y \sim \mathcal{O}(1)$  is preferred by dark matter relic density. Such large Yukawa coupling has a dominant contribution to the evolution of parameter  $m_\eta^2$  [15, 74]

$$Q \frac{dm_\eta^2}{dQ} \simeq \frac{1}{16\pi^2} \left[ 2\text{Tr}(y^\dagger y) m_\eta^2 - 4 \sum_{i=1}^3 M_i^2 (yy^\dagger)_{ii} \right], \quad (2.11)$$

where  $Q$  is the renormalization scale. The second term seems can drive  $m_\eta^2$  to negative, thus breaking the  $Z_2$  symmetry spontaneously. However, as shown in Ref. [74], no spontaneous  $Z_2$  breaking occurs when considering the thermal effects. Meanwhile, the large Yukawa coupling can greatly affect the vacuum stability conditions in Equation (2.2). The most dangerous one is the evolution of parameter  $\lambda_2$  [15]

$$Q \frac{d\lambda_2}{dQ} \simeq \frac{1}{16\pi^2} [12\lambda_2^2 - 4\text{Tr}(y^\dagger y y^\dagger y)]. \quad (2.12)$$

In the limit  $\lambda_2^2 \ll \text{Tr}(y^\dagger y y^\dagger y)$  and assuming constant Yukawa coupling, we can obtain an approximate solution as  $\lambda_2(Q) \simeq \lambda_2(Q_0) - \text{Tr}(y^\dagger y y^\dagger y) \times \log(Q/Q_0)/4\pi^2$ . By setting  $\lambda_2(Q) = 0$ , we then have  $\log(Q/Q_0) = 4\pi^2 \lambda_2(Q_0)/\text{Tr}(y^\dagger y y^\dagger y)$ . Typically for  $\lambda_2(Q_0 = 1 \text{ TeV}) = 0.1$  and  $y \sim \mathcal{O}(1)$ , we have  $Q/Q_0 \sim 50$ , which indicates that Equation (2.2) is only valid up to about 50 TeV. To avoid the  $Z_2$  symmetry breaking and vacuum unstable at high scale, additional scalar that couples strongly to the inert doublet  $\eta$  might be further introduced.

### 3 Lepton Flavor Violation

With TeV-scale new particles in the Scotogeinc model, the Yukawa interaction  $y_{i\alpha}\overline{N}_i\tilde{\eta}^\dagger L_\alpha$  would also induce observable lepton flavor violation (LFV) processes. Here, we briefly summarize the results of experimental limits and theoretical prediction. A detailed discussion has been performed in Ref. [36]. One well-studied process is the radiative decay  $\ell_\alpha \rightarrow \ell_\beta\gamma$ . Currently, the experimental limits on such processes are  $\text{BR}(\mu \rightarrow e\gamma) < 4.2 \times 10^{-13}$  [80],  $\text{BR}(\tau \rightarrow e\gamma) < 3.3 \times 10^{-8}$  [81], and  $\text{BR}(\tau \rightarrow \mu\gamma) < 4.4 \times 10^{-8}$  [81]. The corresponding branching ratios are calculated as [36]

$$\text{BR}(\ell_\alpha \rightarrow \ell_\beta\gamma) = \frac{3(4\pi)^3\alpha}{4G_F^2}|A_D|^2\text{BR}(\ell_\alpha \rightarrow \ell_\beta\nu_\alpha\bar{\nu}_\beta), \quad (3.1)$$

with the dipole form factor

$$A_D = \sum_{i=1}^3 \frac{y_{i\beta}^* y_{i\alpha}}{2(4\pi)^2 M_{\eta^\pm}^2} F_2(\xi_i). \quad (3.2)$$

Here  $\xi_i = M_i^2/M_{\eta^\pm}^2$ , and the loop function  $F_2(x)$  is given by

$$F_2(x) = \frac{1 - 6x + 3x^2 + 2x^3 - 6x^2 \log x}{6(1-x)^4}. \quad (3.3)$$

The three-body decay  $\ell_\alpha \rightarrow 3\ell_\beta$  is also a competitive process. The present limits are  $\text{BR}(\mu \rightarrow 3e) < 1.2 \times 10^{-12}$  [82],  $\text{BR}(\tau \rightarrow 3e) < 2.7 \times 10^{-8}$  [83], and  $\text{BR}(\tau \rightarrow 3\mu) < 2.1 \times 10^{-8}$  [83]. In the Scotogenic model, the dominant contributions are  $\gamma$ -penguins and box diagrams [84]. Meanwhile, the  $Z$ -penguins and Higgs-penguins contributions are suppressed. The branching ratios are given by

$$\begin{aligned} \text{BR}(\ell_\alpha \rightarrow 3\ell_\beta) = & \frac{3(4\pi)^2\alpha^2}{8G_F^2} \left[ |A_{ND}|^2 + |A_D|^2 \left( \frac{16}{3} \log\left(\frac{m_\alpha}{m_\beta}\right) - \frac{22}{3} \right) + \frac{1}{6}|B|^2 \right] \\ & + \left( -2A_{ND}A_D^* + \frac{1}{3}A_{ND}B^* - \frac{2}{3}A_DB^* + \text{h.c.} \right) \text{BR}(\ell_\alpha \rightarrow \ell_\beta\nu_\alpha\bar{\nu}_\beta), \end{aligned} \quad (3.4)$$

with the non-dipole form factor

$$A_{ND} = \sum_{i=1}^3 \frac{y_{i\beta}^* y_{i\alpha}}{6(4\pi)^2 M_{\eta^\pm}^2} G_2(\xi_i), \quad (3.5)$$

and the loop function  $G_2(x)$

$$G_2(x) = \frac{2 - 9x + 18x^2 - 11x^3 + 6x^3 \log x}{6(1-x)^4}. \quad (3.6)$$

The contribution of box diagram  $B$  is

$$e^2 B = \frac{1}{(4\pi)^2 M_{\eta^\pm}^2} \sum_{i,j=1}^3 \left[ \frac{1}{2} D_1(\xi_i, \xi_j) y_{j\beta}^* y_{j\beta} y_{j\beta}^* y_{j\beta} y_{i\alpha} + \sqrt{\xi_i \xi_j} D_2(\xi_i, \xi_j) y_{j\beta}^* y_{j\beta}^* y_{j\beta} y_{i\alpha} \right], \quad (3.7)$$

with the loop function  $D_1(x, y), D_2(x, y)$  of the form

$$D_1(x, y) = -\frac{1}{(1-x)(1-y)} - \frac{x^2 \log x}{(1-x)^2(x-y)} - \frac{y^2 \log y}{(1-y)^2(y-x)}, \quad (3.8)$$

$$D_2(x, y) = -\frac{1}{(1-x)(1-y)} - \frac{x \log x}{(1-x)^2(x-y)} - \frac{y \log y}{(1-y)^2(y-x)}. \quad (3.9)$$

Finally, we consider  $\mu-e$  conversion in nuclei. The most stringent limits are  $\text{CR}(\mu, \text{Ti} \rightarrow e, \text{Ti}) < 4.3 \times 10^{-12}$  [85] and  $\text{CR}(\mu, \text{Au} \rightarrow e, \text{Au}) < 7 \times 10^{-13}$  [86]. The  $\mu-e$  conversion rates, normalized to the muon capture rate  $\Gamma_{\text{capt}}$ , are expressed as

$$\text{CR}(\mu - e, \text{Nucleus}) \simeq \frac{p_e E_e m_\mu^3 G_F^2 \alpha^3 Z_{\text{eff}}^4 F_p^2}{8\pi^2 Z \Gamma_{\text{capt}}} \left| (Z + N)g_{LV}^{(+)} + (Z - N)g_{LV}^{(-)} \right|^2. \quad (3.10)$$

Here,  $p_e \simeq E_e \simeq m_\mu$  are the momentum and energy of the electron.  $Z_{\text{eff}}$  is the effective atomic charge, and  $F_p$  is the nuclear matrix element [87].  $Z$  and  $N$  are the number of protons and neutrons in the nucleus. In the above approximation, we only take into account the left-hand vector effective operators, because contributions from scalar and right-hand vector effective operators are suppressed in the Scotogenic model [36, 37]. The factors  $g_{LV}^{(\pm)}$  are calculated as

$$g_{LV}^{(\pm)} = \frac{1}{2} \sum_{q=u,d,s} \left( g_{LV(q)} G_V^{(q,p)} \pm g_{LV(q)} G_V^{(q,n)} \right). \quad (3.11)$$

The numerical values of the  $G_V$  coefficients are  $G_V^{u,p} = G_V^{(d,n)} = 2, G_V^{d,p} = G_V^{(u,n)} = 1$  [88]. The effective coupling  $g_{LV(q)}$  is dominant by the  $\gamma$ -penguins

$$g_{LV(q)} \approx g_{LV(q)}^\gamma = \frac{\sqrt{2}}{G_F} e^2 Q_q (A_{ND} - A_D), \quad (3.12)$$

with  $Q_q$  the electric charge of the corresponding quark.

With new source of CP-violation, the Yukawa interaction  $y \bar{N} \tilde{\eta}^\dagger L$  contributes to the electric dipole moment (EDM) of charged leptons  $d_\ell$  at two-loop level [89]. An order of magnitude estimation of  $d_\ell$  gives [89]

$$\frac{d_\ell}{e} \sim \frac{m_\ell \lambda_3 \text{Im}(y^2)}{(16\pi^2)^2 M_{\eta^\pm}^2}. \quad (3.13)$$

Provided  $\lambda_3 = 0.01, M_{\eta^\pm} = 3 \text{ TeV}$  and  $\text{Im}(y) \sim \mathcal{O}(1)$ , we have  $d_e/e \sim 4.5 \times 10^{-31} \text{ cm}$ . Such result is much smaller than current experimental bound  $d_e/e < 8.7 \times 10^{-29} \text{ cm}$  [90]. So the EDM limit is easy to satisfy.

## 4 Dark Matter

In this paper, we assume  $N_1$  as the dark matter candidate in the freeze-out scenario. We only consider the pair annihilation channels  $N_1 N_1 \rightarrow \ell^+ \ell^-, \bar{\nu} \nu$ . For a compressed mass

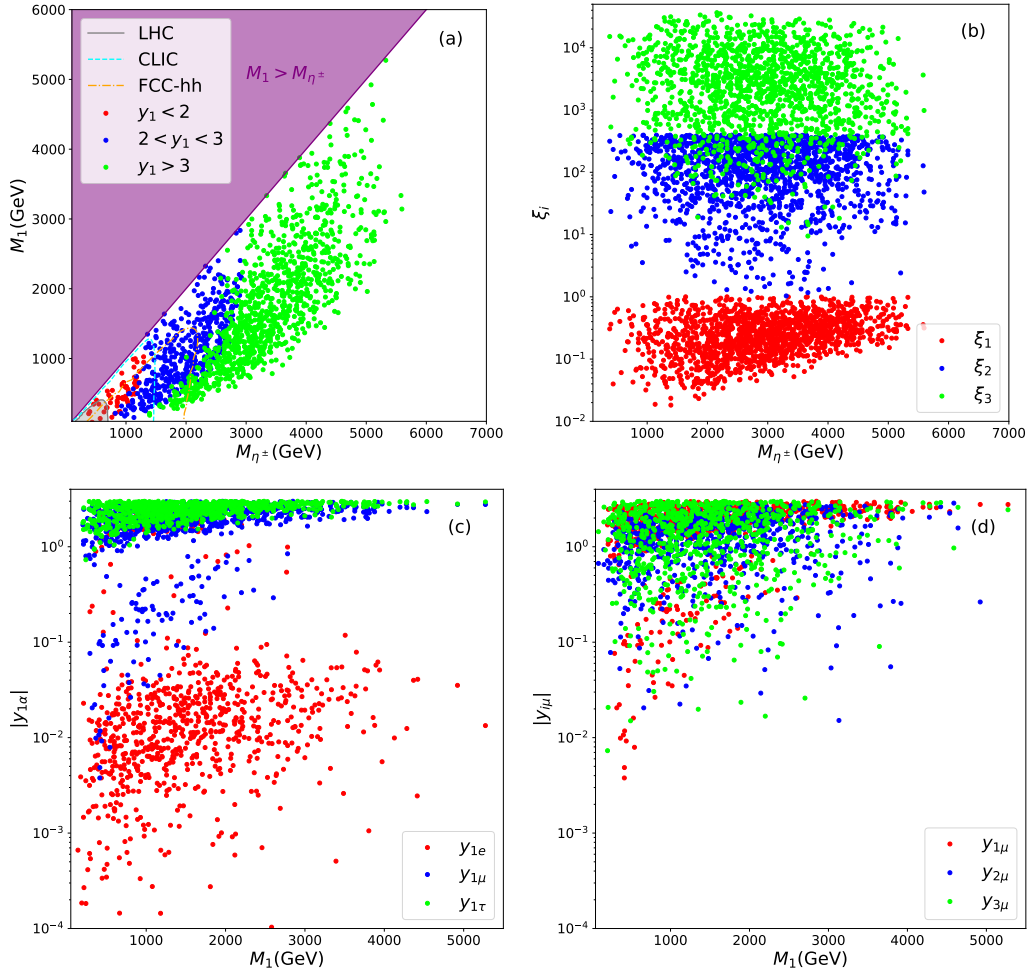


**Figure 2.** The allowed samples under constraints from lepton flavor violation and dark matter relic density. The gray region in panel (a) is excluded by LHC [39]. The cyan and orange lines correspond to the future limits by CLIC and FCC-hh [38].

spectrum  $M_1 \sim M_{\eta^\pm}$ , the  $N_1\eta$  coannihilation channels are also possible and may become dominant [37]. Provided vanishing lepton masses, the pair annihilation cross-section in powers of the relative dark matter velocity ( $v_r$ ) is [9]

$$\sigma v_r = 0 + \frac{y_1^4 r_1^2 (1 - 2r_1 + 2r_1^4)}{24\pi M_1^2} v_r^2 \equiv a + b v_r^2, \quad (4.1)$$

where  $y_1^4 = \sum_{\alpha\beta} |y_{1\alpha} y_{1\beta}^*|^2$ ,  $r_1 = M_1^2 / (M_{\eta^\pm}^2 + M_1^2)$ . For simplicity, we assume masses of inert scalars are degenerate  $M_{\eta^\pm} \simeq M_R \simeq M_I$ . The thermally averaged cross-section can be calculated as  $\langle \sigma v_r \rangle = a + 6b/x_f$ . Then we can obtain the freeze-out parameter  $x_f$  by numerically solving

$$x_f = \log \frac{0.0764c(2+c)M_{\text{Pl}}M_1 6b/x_f}{\sqrt{g_* x_f}}, \quad (4.2)$$

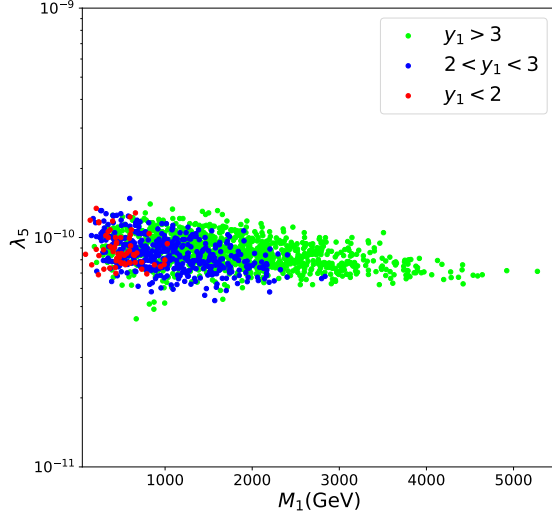


**Figure 3.** Same as Figure 2, but in the  $M_1 - \lambda_5$  plane.

where  $c \simeq 1/2$ ,  $M_{\text{Pl}} = 1.22 \times 10^{19}$  GeV, and  $g_*$  is the number of relativistic degrees of freedom. The final dark matter relic density is calculated as

$$\Omega h^2 = \frac{1.07 \times 10^9 \text{GeV}^{-1}}{M_{\text{Pl}}} \frac{x_f}{\sqrt{g_*}} \frac{1}{a + 3b/x_f}. \quad (4.3)$$

For the fermion dark matter  $N_1$ , the interactions with nucleons appear at the one-loop level. As already discussed in Ref. [35], the spin-independent cross-section via the Higgs exchange is

$$\sigma_{\text{SI}} = \frac{4}{\pi} \frac{M_1^2 m_p^2}{(M_1 + m_p)^2} m_p^2 \left( \frac{\Lambda_q}{m_q} \right)^2 f_p^2, \quad (4.4)$$

where  $m_p$  is the proton mass,  $f_p \approx 0.3$  is the scalar form factor, and the effective scalar coupling  $\Lambda_q$  is

$$\Lambda_q = -\frac{y_1^2}{16\pi^2 M_h^2 M_1} \left[ \lambda_3 G_1 \left( \frac{M_1^2}{M_{\eta^\pm}^2} \right) + \frac{\lambda_3 + \lambda_4}{2} G_1 \left( \frac{M_1^2}{M_{R,I}^2} \right) \right] m_q, \quad (4.5)$$

with the loop function  $G_1(x)$  defined as

$$G_1(x) = \frac{x + (1-x) \log(1-x)}{x}. \quad (4.6)$$

To make sure the explored parameter space is safe under the tight constraints from direct detection [91, 92], we assume the couplings  $\lambda_{3,4} = 0.01$  in the following study [35].

Since the neutrino mass, lepton flavor violation, and dark matter relic density involve the same Yukawa interactions, a combined analysis is required to explore the parameter space. Based on the strategy in Ref. [37], we perform a random scan over the following

	$M_1$	$M_2$	$M_3$	$M_{\eta^\pm}$	$ y_{1e} $	$ y_{1\mu} $	$ y_{1\tau} $	$\Omega h^2$
BP-1	648.7	$5.06 \times 10^3$	$3.39 \times 10^4$	1141	$2.62 \times 10^{-2}$	1.17	1.49	0.122
BP-2	1579	$1.82 \times 10^4$	$1.22 \times 10^5$	2647	$9.05 \times 10^{-4}$	1.99	2.08	0.123
BP-3	2521	$6.30 \times 10^4$	$5.52 \times 10^5$	4371	$2.17 \times 10^{-2}$	2.31	2.95	0.121

**Table 1.** Benchmark points for MuC studies. Here, all the masses are in the unit of GeV.

parameter space:

$$\begin{aligned}
M_1 &\in [100, 10000] \text{ GeV}, M_{\eta^\pm} \in [100, 10000] \text{ GeV}, \\
M_2 &\in [M_1, 20M_{\eta^\pm}], M_3 \in [M_2, 200M_{\eta^\pm}], \lambda_5 \in [10^{-11}, 10^{-9}].
\end{aligned}
\tag{4.7}$$

During the scan, we assume flat prior distributions for all the parameters.

For  $M_1 < 100$  GeV, the parameter space has been mostly excluded by lepton flavor violation [37] and direct search at LHC [39–41], thus this region is not considered in this work. Slightly different from the previous study in Ref. [37], the upper bounds on the heavier singlet fermions  $N_2$  and  $N_3$  are much higher in our studies. The viable samples are required to satisfy current LFV bounds and predict the correct dark matter relic density as well [93]. During the scan, we also impose a perturbativity limit on the Yukawa couplings  $|y_{i\alpha}| < 3$ .

The allowed samples and possible collider limits are shown in Figure 2 and 3. From the distribution in the  $M_{\eta^\pm} - M_1$  plane, it is clear that the allowed region satisfies  $M_{\eta^\pm} \lesssim 5.5$  TeV and  $M_1 \lesssim 5$  TeV. In Figure 2 (a), the excluded regions by current LHC, future CLIC and FCC-hh are also shown. The current LHC exclusion region only covers a small portion of the parameter space. The CLIC has the potential to cover the whole region with  $y_1 < 2$ . Meanwhile, FCC-hh could probe the region  $M_{\eta^\pm} \lesssim 2$  TeV with most samples satisfying  $y_1 \lesssim 3$ . For samples with  $y_1 \gtrsim 3$ , most of them are beyond the reach of LHC, CLIC and FCC-hh. However, as will be shown later, such samples can be easily probed at a multi-TeV MuC. The parameter  $\xi_i = M_i^2/M_{\eta^\pm}^2$  is shown in Figure 2 (b). We notice that the upper bounds on  $\xi_i$  shown in Figure 4 of Ref. [37] actually correspond to the requirements  $M_{2(3)} < 5(10)$  TeV. Therefore, by allowing much larger values of  $M_{2,3}$ , we obtain a wider parameter space in the  $M_{\eta^\pm} - M_1$  plane. Our results imply that  $M_1 < M_{\eta^\pm} < M_2 < M_3$  is the favored mass spectrum for TeV-scale  $M_1$ . In Figure 2 (c), the distributions of  $|y_{1\alpha}|$ , which is correlated with LFV and relic density, are shown. The TeV scale dark matter usually requires a hierarchical structure  $|y_{1e}| \ll |y_{1\mu}| \sim |y_{1\tau}|$  with  $|y_{1e}| \lesssim 0.1, 1 \lesssim |y_{1\mu}| \lesssim |y_{1\tau}|$ . Hence, the dark matter  $N_1$  and inert charged scalar  $\eta^\pm$  behave as  $\mu\tau$ -philic particles. As a complementary, the  $\mu$ -related Yukawa couplings  $|y_{i\mu}|$  are also depicted in Figure 2 (d), which are involved in the production of  $\eta^+\eta^-$  at MuC. Most samples predict  $|y_{i\mu}| \gtrsim 0.1$  without any special hierarchical structure. With sizable

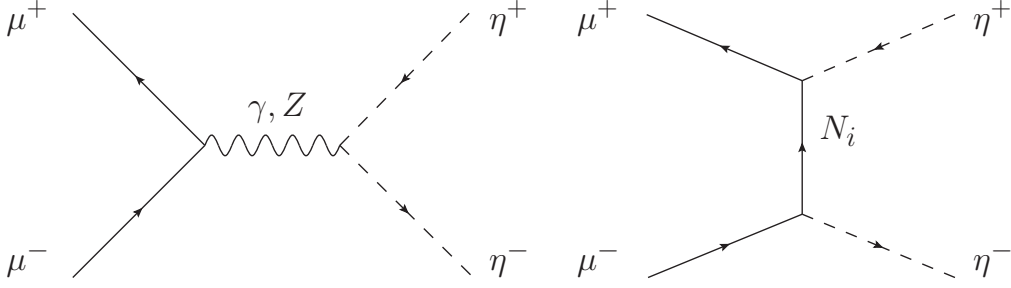


**Figure 4.** Charged scalar pair production at the muon collider.

Yukawa couplings, correct neutrino mass can still be obtained by tiny  $\lambda_5$ . In Figure 3, the allowed values of  $\lambda_5$  are shown, which indicates that  $\lambda_5 \sim 10^{-10}$  should be satisfied.

Based on the above discussion, we have selected three benchmark points (BP) for the following MuC studies. Detailed information of the BPs are listed in Table 1. BP-1 is also within the reach of CLIC and FCC-hh, while BP-2 and BP-3 are out reach of them. Notably,  $|y_{1\tau}| = 2.954$  in BP-3 is close to the upper bound of the perturbativity limit  $|y_{i\alpha}| < 3$ .

## 5 Signatures at Muon Collider

In this section, we investigate the signatures of the Scotogenic model at a multi-TeV MuC, which is well motivated due to large  $\mu$ -related Yukawa coupling. As shown in Figure 4, the charged scalar  $\eta^\pm$  can be pair produced via the  $s$ -channel exchange of  $\gamma/Z$  boson, and via the  $t$ -channel exchange of  $N_i$ . The corresponding production cross-section is then calculated as [94]

$$\sigma(\mu^+\mu^-\rightarrow\eta^+\eta^-)=\frac{\pi\alpha^2}{s}\left\{\frac{1}{3}\beta^3\left[1+g_L(g_L+g_R)\frac{s}{s-M_Z^2}+g_L^2(g_L^2+g_R^2)\frac{s^2}{(s-M_Z^2)^2}\right]\right. \\ \left.+\sum_{i=1}^3\sum_{j=1}^3\frac{|y_{i\mu}|^2|y_{j\mu}|^2}{64\pi^2\alpha^2}H_{ij}+\sum_{i=1}^3\frac{|y_{i\mu}|^2}{8\pi\alpha}\left[1+g_L^2\frac{s}{s-M_Z^2}\right]F_i\right\}, \quad (5.1)$$

where the left- and right-chiral  $Z$  couplings are

$$g_L=\frac{-1+2s_W^2}{2s_Wc_W}, g_R=\frac{s_W}{c_W}, \quad (5.2)$$

with  $s_W = \sin\theta_W$ ,  $c_W = \cos\theta_W$ , and  $\theta_W$  is the weak mixing angle. The kinematical functions  $H_{ij}$  and  $F_i$  read

$$H_{ij}=\begin{cases} -2\beta+\Delta_i\ln\frac{\Delta_i+\beta}{\Delta_i-\beta} & i=j \\ \frac{F_j-F_i}{\Delta_i-\Delta_j} & i\neq j \end{cases}, \quad (5.3)$$

$$F_i=\Delta_i\beta-\frac{\Delta_i^2-\beta^2}{2}\ln\frac{\Delta_i+\beta}{\Delta_i-\beta}, \quad (5.4)$$

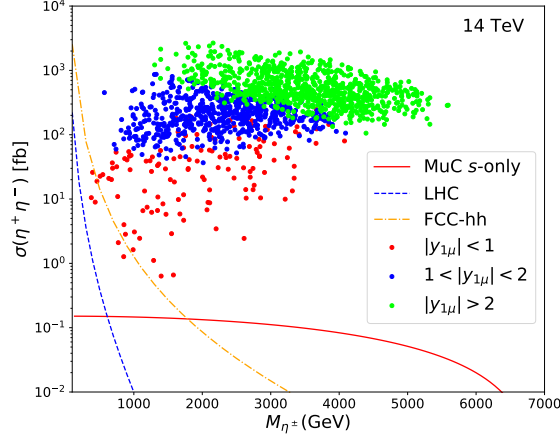


**Figure 5.** The production cross-section of  $\mu^+\mu^- \rightarrow \eta^+\eta^-$  at 14 TeV MuC. The red solid line is the cross-section at MuC with  $s$ -channel contribution only. The blue dashed (yellow dash-dotted) line corresponds to cross-section at 14 TeV LHC (100 TeV FCC-hh).

where the parameters  $\Delta_i$  and  $\beta$  are given by

$$\Delta_i = \frac{2}{s}(M_{\eta^\pm}^2 - M_i^2) - 1, \beta = \sqrt{1 - 4M_{\eta^\pm}^2/s}. \quad (5.5)$$

The theoretically predicted production cross-section  $\sigma(\eta^+\eta^-)$  at 14 TeV MuC is shown in Figure 5. It is obvious that the cross-section can be greatly enhanced by the  $t$ -channel contribution. The strong correlation between  $\sigma(\eta^+\eta^-)$  and  $|y_{1\mu}|$  indicates that the  $t$ -channel exchange of  $N_1$  is the dominant contribution. Compared with the  $s$ -channel, the enhancement factor due to the  $t$ -channel might be naively estimated as  $|y_{1\mu}|^4/(16\pi^2\alpha^2)$ , e.g.,  $|y_{1\mu}| = 2$  leading to an enhancement factor at the order of  $\sim 2000$ . For a fixed value of  $|y_{1\mu}|$ ,  $\sigma(\eta^+\eta^-)$  tends to decrease as  $M_{\eta^\pm}$  increases. Meanwhile, as the lower limits on  $|y_{1\mu}|$  becomes higher when  $\eta^\pm$  is heavier, the resulting predicted lower bounds of  $\sigma(\eta^+\eta^-)$  will increase. The  $\sigma(\eta^+\eta^-)$  could reach a maximum value of about 3000 fb with  $M_{\eta^\pm} \sim 2$  TeV. For charged scalar  $\eta^\pm$  heavier than 4 TeV, the  $\sigma(\eta^+\eta^-)$  is roughly in the range of [100,1000] fb with  $|y_{1\mu}| > 2$ . When  $|y_{1\mu}| > 1$ , the  $\sigma(\eta^+\eta^-) \gtrsim 100$  fb is always expected. Samples with  $|y_{1\mu}| < 1$  usually predict a cross-section smaller than 100 fb, where contributions from  $N_{2,3}$  may become important if  $|y_{1\mu}|$  is too small. All the samples lead to a larger cross-section at MuC than at LHC. Only a few samples with  $M_{\eta^\pm} \lesssim 1000$  GeV and  $|y_{1\mu}| < 1$  have a cross-section at MuC smaller than at FCC-hh. Actually, for  $M_{\eta^\pm} \gtrsim 1800$  GeV, the cross-section at MuC with only  $s$ -channel contribution is larger than at FCC-hh.

Now we consider the decays of charged scalar  $\eta^\pm$ . The corresponding decay width is

$$\Gamma(\eta^\pm \rightarrow \ell_\alpha^\pm N_i) = \frac{|y_{i\alpha}|^2}{16\pi} M_{\eta^\pm} \left(1 - \frac{M_i^2}{M_{\eta^\pm}^2}\right)^2. \quad (5.6)$$

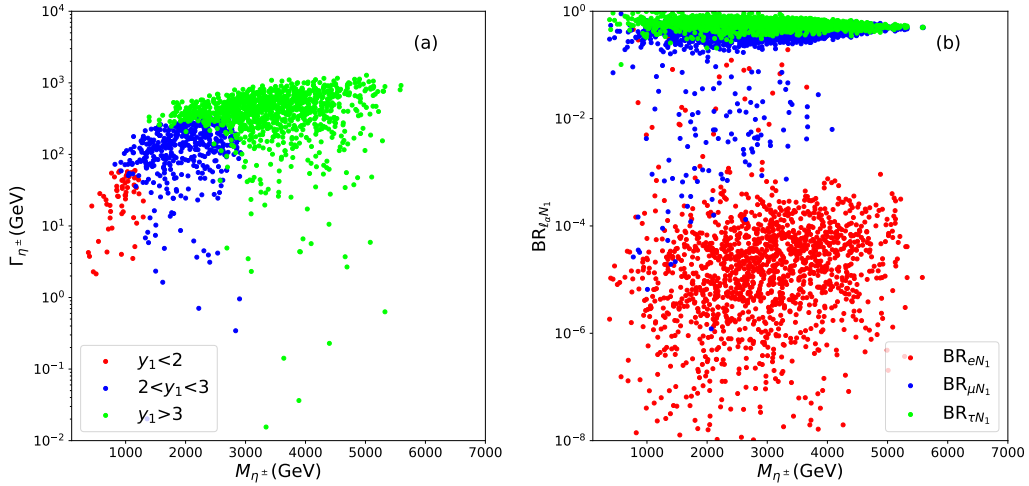


**Figure 6.** Left: The total decay width of charged scalar  $\eta^\pm$ . Right: The branching ratios of charged scalar  $\eta^\pm$ .

In principle,  $\eta^\pm$  can decay into all three generations of  $N_i$ . However, our scanned samples favor the spectrum  $M_1 < M_{\eta^\pm} < M_2 < M_3$ , which means  $\eta^\pm$  can only decay into  $N_1$  via  $\eta^\pm \rightarrow \ell_\alpha^\pm N_1$ . The total decay width  $\Gamma_{\eta^\pm}$  and branching ratios are shown in Figure 6. The total decay width  $\Gamma_{\eta^\pm}$  can be as large as 1 TeV with  $y_1 > 3$ . Meanwhile for  $y_1 < 2$ , the total decay width is less than 100 GeV. Suppression of  $\Gamma_{\eta^\pm}$  is also possible with compressed spectrum  $M_1 \sim M_{\eta^\pm}$ . With hierarchical Yukawa couplings  $|y_{1e}| \ll |y_{1\mu}| \sim |y_{1\tau}|$ , the corresponding branching ratios are also hierarchical, i.e.,  $\text{BR}_{eN_1} \ll \text{BR}_{\mu N_1} \lesssim \text{BR}_{\tau N_1}$ . The  $\tau$  final state has a branching ratio always larger than 0.2. Most samples predict  $\text{BR}_{\mu N_1} \gtrsim 10^{-2}$  and  $\text{BR}_{eN_1} \lesssim 10^{-4}$ .

### 5.1 $\mu^+\mu^- + \cancel{E}_T$ Signature

The usual dilepton signature considers both electron and muon final states. However, in the Scotogenic model, the  $\text{BR}_{eN_1}$  is suppressed by tiny  $|y_{1e}|$ . So we only consider the muon channel. The explicit opposite-sign dimuon signature at MuC is

$$\mu^+\mu^- \rightarrow \eta^+\eta^- \rightarrow \mu^+N_1 + \mu^-N_1 \rightarrow \mu^+\mu^- + \cancel{E}_T. \quad (5.7)$$

The corresponding backgrounds are

$$\mu^+\mu^- \rightarrow \mu^+\mu^-, \mu^+\mu^- \bar{\nu}_\ell \nu_\ell, W^+W^- \bar{\nu}_\ell \nu_\ell, \quad (5.8)$$

with the leptonic decay  $W^\pm \rightarrow \mu^\pm \nu_\mu$  and  $\nu_\ell = \nu_{e,\mu,\tau}$  including all flavors. Here, the  $\mu^+\mu^- \rightarrow W^+W^- \bar{\nu}_\ell \nu_\ell$  is dominant by the VBF process [95–97]. The dimuon signature and corresponding backgrounds are simulated with **MadGraph5\_aMC@NLO** [98]. The detector effects are illustrated by using **Delphes** [99] with the parameters in the delphes\_card\_MuonColliderDet.tcl card. In this paper, we perform a simple cut-based

$\sigma(\text{fb})$	<b>BP-1</b>	<b>BP-2</b>	<b>BP-3</b>	$\mu^+\mu^-$	$\mu^+\mu^-\bar{\nu}_\ell\nu_\ell$	$W^+W^-\bar{\nu}_\ell\nu_\ell$
Preselection	19.7	93.8	35.1	220	93.4	6.41
$N_{\mu^\pm} = 1$ $P_T^{\mu^\pm} > 10 \text{ GeV}$	8.10	40.6	12.9	69.7	69.3	2.25
$\cancel{E}_T > 300 \text{ GeV}$	7.08	38.7	12.5	52.3	16.5	0.63
$ \pi - \theta_{\mu^+} - \theta_{\mu^-}  > 0.0016$	7.03	38.6	12.5	0.00	16.5	0.63
$ \eta_{\mu^\pm}  < 2$	5.86	34.5	11.7	0.00	11.1	0.52
$E_{\mu^+} + E_{\mu^-} > 2 \text{ TeV}$	4.90	29.6	11.0	0.00	1.95	0.10
$M_{\mu^+\mu^-} > 1 \text{ TeV}$	4.77	28.4	10.2	0.00	1.23	0.06
$ \vec{P}_{\mu^+} + \vec{P}_{\mu^-}  < 3.5 \text{ TeV}$	4.51	26.2	8.50	0.00	0.15	0.06
Significance	29.4	72.1	40.7	Total Background		0.21
$5\sigma$ Luminosity ( $\text{fb}^{-1}$ )	5.80	0.96	3.01			

**Table 2.** Cut flow table for the dimuon signature  $\mu^+\mu^- + \cancel{E}_T$  from BP-1, BP-2, BP-3, and various background processes at the  $\sqrt{s} = 14 \text{ TeV}$  MuC. The significance  $S/\sqrt{S+B}$  is calculated by assuming an integrated luminosity  $\mathcal{L} = 200 \text{ fb}^{-1}$ .

analysis of the signature. The cut flow for the dimuon signature and backgrounds are summarized in Table 2.

First, we select events with exact two opposite-sign muons via the following cuts

$$N_{\mu^\pm} = 1, P_T^{\mu^\pm} > 10 \text{ GeV}. \quad (5.9)$$

Because the dark matter  $N_1$  is invisible at detectors, the missing transverse energy  $\cancel{E}_T$  is the characteristic feature of this signal. Distributions of  $\cancel{E}_T$  for the signals and backgrounds are shown in the up-left panel of Figure 7. The signals tend to have larger  $\cancel{E}_T$  than the backgrounds. In our analysis, we require a relatively large  $\cancel{E}_T$  to suppress the backgrounds

$$\cancel{E}_T > 300 \text{ GeV}. \quad (5.10)$$

At this level, the cross-section of the  $\mu^+\mu^- \rightarrow \mu^+\mu^-$  channel is still quite large. To dig signal events from background events, further cuts should be applied. The normalized distribution of relevant parameters are also shown in Figure 7. From the distribution of dimuon acollinearity  $\theta_{\mu^+} + \theta_{\mu^-}$  in the up-right panel, it is clear that the corresponding out-going muons in the  $\mu^+\mu^-$  channel are back-to-back. Therefore, this background can be easily suppressed to a negligible level by the requirement

$$|\pi - \theta_{\mu^+} - \theta_{\mu^-}| > 0.0016. \quad (5.11)$$

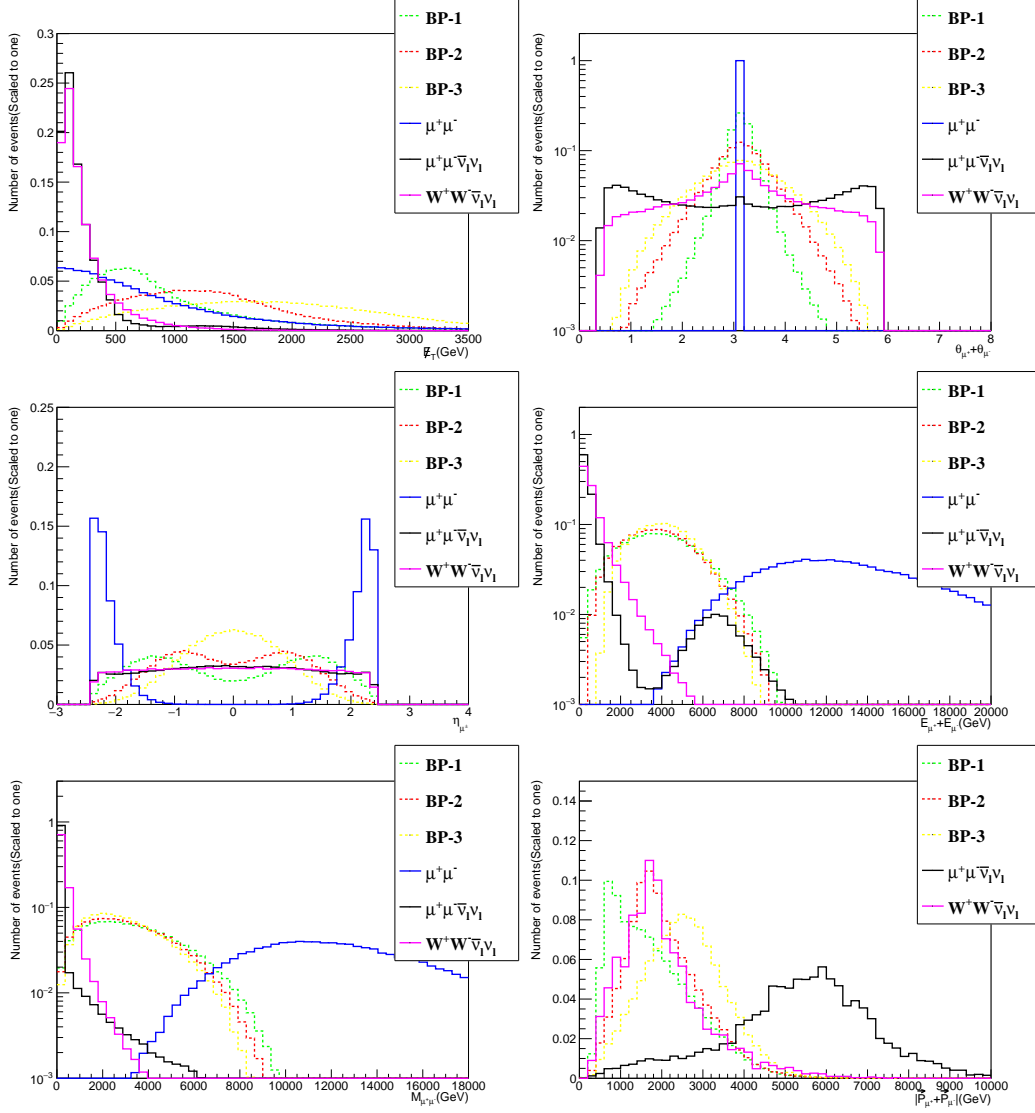


**Figure 7.** Normalized distribution of missing transverse energy  $\cancel{E}_T$  (up-left panel), dimuon acollinearity  $\theta_{\mu^+} + \theta_{\mu^-}$  (up-right panel), pseudorapidity  $\eta_{\mu^\pm}$  (middle-left panel), dimuon energy  $E_{\mu^+} + E_{\mu^-}$  (middle-right panel), dimuon invariant mass  $M_{\mu^+\mu^-}$  (down-left panel), vector sum momentum of dimuon  $|\vec{P}_{\mu^+} + \vec{P}_{\mu^-}|$  (down-right panel) for benchmark points (dashed lines) and corresponding backgrounds (solid lines) at the  $s = \sqrt{14}$  TeV muon collider. Variable  $|\vec{P}_{\mu^+} + \vec{P}_{\mu^-}|$  is shown after applying cuts from Equation (5.9) to (5.14), while the other five variables are shown with only the cuts in Equation (5.9).

After suppressing  $\mu^+\mu^-$ , the  $\mu^+\mu^-\bar{\nu}_\ell\nu_\ell$  channel with a cross-section of 15.0 fb becomes the dominant one, which is already smaller than the cross-section of BP-2. In order to determine the masses of charged-scalar  $\eta^\pm$  and dark matter  $N_1$  more precisely, we try to eliminate the backgrounds as small as possible. In the distribution of pseudorapidity  $\eta_{\mu^\pm}$  in the middle-left panel of Figure 7, the background  $\mu^+\mu^-\bar{\nu}_\ell\nu_\ell$  has a nearly flat distribution,

so we tighten the events with the cut

$$|\eta_{\mu^\pm}| < 2. \quad (5.12)$$

As shown in the middle-right panel of Figure 7, the dimuon energy  $E_{\mu^+} + E_{\mu^-}$  of the backgrounds  $\mu^+\mu^-\bar{\nu}_\ell\nu_\ell$  and  $W^+W^-\bar{\nu}_\ell\nu_\ell$  are typically less than 2 TeV, while the signals are in the range of 1  $\sim$  9 TeV. So we require

$$E_{\mu^+} + E_{\mu^-} > 2 \text{ TeV}. \quad (5.13)$$

Notably, there are a few parts of the  $\mu^+\mu^-\bar{\nu}_\ell\nu_\ell$  samples leading to  $E_{\mu^+} + E_{\mu^-}$  in 4  $\sim$  9 TeV, which is overlap with the signals. We do not apply an upper bound on  $E_{\mu^+} + E_{\mu^-}$ , because the energetic  $\mu^+\mu^-$  background has already been suppressed to zero by the cut on the dimuon acollinearity in Equation (5.11). Another distinguishable viable is the dimuon invariant mass  $M_{\mu^+\mu^-}$  as shown in the down-left panel of Figure 7. About 90% of the  $\mu^+\mu^-\bar{\nu}_\ell\nu_\ell$  samples have an invariant mass  $M_{\mu^+\mu^-}$  less than 100 GeV, which is due to such samples produced from the on-shell decay of  $Z$  boson. For the  $W^+W^-\bar{\nu}_\ell\nu_\ell$  background, it usually leads to  $M_{\mu^+\mu^-} < 1$  TeV. And most of the signal samples predict  $M_{\mu^+\mu^-} \in [0, 8]$  TeV. Based on this distribution, we then apply the cut

$$M_{\mu^+\mu^-} > 1 \text{ TeV}. \quad (5.14)$$

In the down-right panel of Figure 7, we illustrate the distribution of vector sum momentum of dimuon  $|\vec{P}_{\mu^+} + \vec{P}_{\mu^-}|$  after applying the cuts from Equation (5.9) to (5.14). The distribution of survived  $\mu^+\mu^-\bar{\nu}_\ell\nu_\ell$  samples has a peak value around 5 to 6 TeV, meanwhile the peak values of signals and  $W^+W^-\bar{\nu}_\ell\nu_\ell$  background are less than 3 TeV. We adopt the cut

$$|\vec{P}_{\mu^+} + \vec{P}_{\mu^-}| < 3.5 \text{ TeV} \quad (5.15)$$

to further suppress the  $\mu^+\mu^-\bar{\nu}_\ell\nu_\ell$  background.

The final cross-sections of signals are 4.51 fb, 26.2 fb, and 8.50 fb for BP-1, BP-2, and BP-3, respectively. The final cross-section of total backgrounds is 0.21 fb, with 0.15 fb from  $\mu^+\mu^-\bar{\nu}_\ell\nu_\ell$  channel and 0.06 fb from  $W^+W^-\bar{\nu}_\ell\nu_\ell$  channel. Provided an integrated luminosity of 200 fb $^{-1}$ , the expected significance will reach 29.4 for BP-1, 72.1 for BP-2, and 40.7 for BP-3. To reach the  $5\sigma$  discovery limit, BP-2 is the most promising one, which only requires about 1 fb $^{-1}$  data. For BP-1 and BP-3, 10 fb $^{-1}$  data will make sure to discover them.

Based on the above cuts in Equation (5.9) - (5.15), we explore the  $5\sigma$  discovery reach at the 14 TeV MuC. For the Scotogenic model at the MuC, both the Yukawa couplings and the mass spectrum will affect the significance. A full simulation and scan over the whole parameter space are beyond the scope of this work. For simplicity, we consider the scenarios with fixed mass relation or fixed Yukawa couplings to qualitatively obtain the discovery reach. The results are shown in Figure 8. First, we assume the mass relation

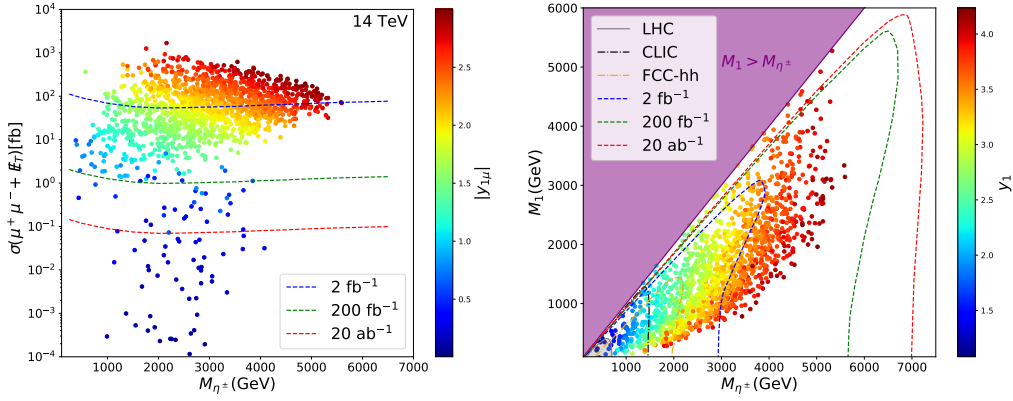


**Figure 8.** The  $5\sigma$  discovery reaches at the 14 TeV MuC for different luminosity. In the left panel, the discovery limits are obtained by assuming  $M_1 = M_{\eta^\pm}/2$ . In the right panel, we have fixed  $y_{1e} = 0.02, y_{1\mu} = y_{1\tau} = 2$  and neglected the contribution of  $N_{2,3}$  to derive the discovery limits. The gray region is excluded by LHC [39]. The black and orange lines are the future limits by CLIC and FCC-hh [38].

$M_1 = M_{\eta^\pm}/2$ . The total cut efficiency is about 0.2 for the signal. In the left panel of Figure 8, we show the  $5\sigma$  discovery reach on the theoretical signal cross-section, which is calculated as

$$\sigma(\mu^+\mu^- + \cancel{E}_T) = \sigma(\eta^+\eta^-) \times \text{BR}_{\mu N_1}^2. \quad (5.16)$$

With  $2 \text{ fb}^{-1}$  data, the 14 TeV MuC is able to probe  $\sigma(\mu^+\mu^- + \cancel{E}_T) \gtrsim 100 \text{ fb}$ , covering the most region with  $|y_{1\mu}| \gtrsim 2$ . The discovery limit is down to about 1 fb, when the integrated luminosity reaches  $200 \text{ fb}^{-1}$ . This will unravel the whole region with  $|y_{1\mu}| \gtrsim 1$ . With  $20 \text{ ab}^{-1}$  data,  $\sigma(\mu^+\mu^- + \cancel{E}_T) \gtrsim 0.1 \text{ fb}$  can be discovered. However, the production cross-section  $\sigma(\eta^+\eta^-)$  and the decay branching ratio  $\text{BR}_{\mu N_1}$  are both suppressed for  $|y_{1\mu}| < 1$ . The theoretical cross-section can be much smaller than 0.1 fb, thus beyond the reach of MuC.

In the right panel of Figure 8, we fix  $y_{1e} = 0.02, y_{1\mu} = y_{1\tau} = 2$  and consider the effect of mass spectrum. It is obvious that the discovery reach of 14 TeV MuC for the Scotogenic model can easily exceed the 100 TeV FCC-hh. Most samples with  $M_{\eta^\pm} \lesssim 3.9 \text{ TeV}$  and  $M_1 \lesssim 2.9 \text{ TeV}$  are within the reach of  $2 \text{ fb}^{-1}$  data. With  $200 \text{ fb}^{-1}$  data, it is able to probe the region with  $M_{\eta^\pm} \lesssim 6.7 \text{ TeV}$  and  $M_1 \lesssim 5.6 \text{ TeV}$ , which almost cover the whole region with correct relic density and satisfying lepton flavor violation. For the compressed mass region  $M_1 \simeq M_{\eta^\pm}$ , the final states muons are relatively soft and become hard to pass through the energetic cut as  $E_{\mu^+} + E_{\mu^-} > 2 \text{ TeV}$ . Therefore, only increasing the integrated luminosity to  $20 \text{ ab}^{-1}$  will not help too much to probe such a region. Because of the large decay width of  $\eta^\pm$ , the  $\eta^\pm$  can still be pair produced via the off-shell process even when  $M_{\eta^\pm} > 7 \text{ TeV}$ . We find that the 14 TeV MuC could probe  $M_{\eta^\pm} \lesssim 7.2 \text{ TeV}$  with  $20 \text{ ab}^{-1}$  data, although such large  $M_{\eta^\pm}$  can not lead to correct relic density.

$\sigma(\text{fb})$	<b>BP-1</b>	<b>BP-2</b>	<b>BP-3</b>	$\tau^+\tau^-$	$\tau^+\tau^-\bar{\nu}_\ell\nu_\ell$	$W^+W^-\bar{\nu}_\ell\nu_\ell$
Preselection	51.9	111	93.9	0.531	102.4	6.405
$N_{\tau^\pm} = 1$ $P_T^{\tau^\pm} > 20 \text{ GeV}$	3.38	7.52	6.34	0.075	8.349	0.278
$\cancel{E}_T > 100 \text{ GeV}$	3.24	7.43	6.30	0.072	4.202	0.162
$ \pi - \theta_{\tau^+} - \theta_{\tau^-}  > 0.04$	2.74	6.93	6.02	0.003	4.149	0.155
$ \eta_{\tau^\pm}  < 2.5$	2.52	6.67	5.89	0.003	4.139	0.153
$E_{\tau^+} + E_{\tau^-} > 1 \text{ TeV}$	2.26	6.04	5.56	0.003	0.246	0.039
$M_{\tau^+\tau^-} > 0.5 \text{ TeV}$	2.22	5.87	5.36	0.003	0.034	0.025
Significance	20.8	34.1	32.6	Total Background		0.062
$5\sigma$ Luminosity ( $\text{fb}^{-1}$ )	11.6	4.30	4.72			

**Table 3.** Same as Table. 2, but for the  $\tau^+\tau^- + \cancel{E}_T$  signature. In this channel, we do not apply cut on  $|\vec{P}_{\tau^+} + \vec{P}_{\tau^-}|$ .

## 5.2 $\tau^+\tau^- + \cancel{E}_T$ Signature

Besides the opposite-sign dimuon signature  $\mu^+\mu^- + \cancel{E}_T$ , the opposite-sign ditau signature  $\tau^+\tau^- + \cancel{E}_T$  are usually less promising due to the lower tau-tagging efficiency [38]. However, with a relatively large branching ratio  $\text{BR}_{\tau N_1} \gtrsim 0.2$ , the ditau signature is expected more promising than the dimuon channel when the latter is suppressed by the branching ratio. In this paper, we consider the hadronic decay of  $\tau$ , and assume the  $\tau$ -tagging efficiency to be 0.4 [100]. The opposite-sign ditau signature at MuC is

$$\mu^+\mu^- \rightarrow \eta^+\eta^- \rightarrow \tau^+N_1 + \tau^-N_1 \rightarrow \tau^+\tau^- + \cancel{E}_T. \quad (5.17)$$

The corresponding backgrounds are from

$$\mu^+\mu^- \rightarrow \tau^+\tau^-, \tau^+\tau^-\bar{\nu}_\ell\nu_\ell, W^+W^-\bar{\nu}_\ell\nu_\ell, \quad (5.18)$$

followed by  $W^\pm \rightarrow \tau^\pm\nu_\tau$ . Different from the  $\mu^+\mu^- \rightarrow \mu^+\mu^-$  process, the  $\mu^+\mu^- \rightarrow \tau^+\tau^-$  only has  $s$ -channel contribution, so  $\sigma(\tau^+\tau^-)$  is relatively small.

First, events with two opposite-sign taus are selected by

$$N_{\tau^\pm} = 1, P_T^{\tau^\pm} > 20 \text{ GeV}. \quad (5.19)$$

Since hadronic decay of  $\tau$  is considered, we require  $P_T^{\tau^\pm} > 20 \text{ GeV}$  to pass the trigger cut. At this level, the dominant background is  $\tau^+\tau^-\bar{\nu}_\ell\nu_\ell$ , which is slightly larger than

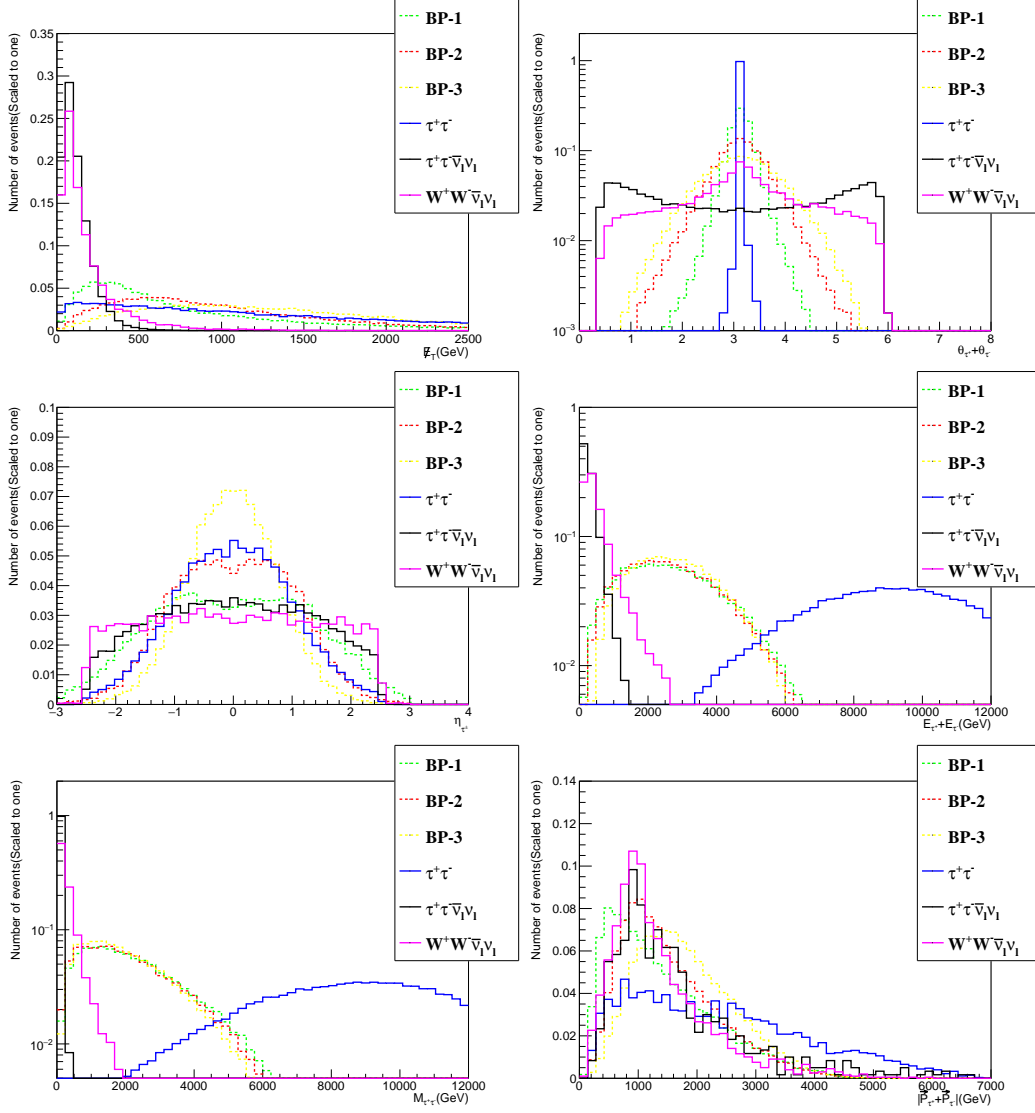


**Figure 9.** Same as Figure 7, but for the ditau signature.

the signal. In Figure 9, the normalized distribution of relevant parameters are shown. Generally speaking, distributions of these variables for the ditau signature are similar to the dimuon signature. The ditau signature thus is analyzed with similar cuts as the dimuon signature. The cut flow for the ditau signature and backgrounds are summarized in Table 3. However, in order to keep as much as the signal events, we lose some cuts compared with the dimuon signal. For instance, we apply the cut

$$\cancel{E}_T > 100 \text{ GeV} \quad (5.20)$$

to select samples with missing transverse energy. After this cut, the total background is already smaller than the cross-section of BP-2 and BP-3.

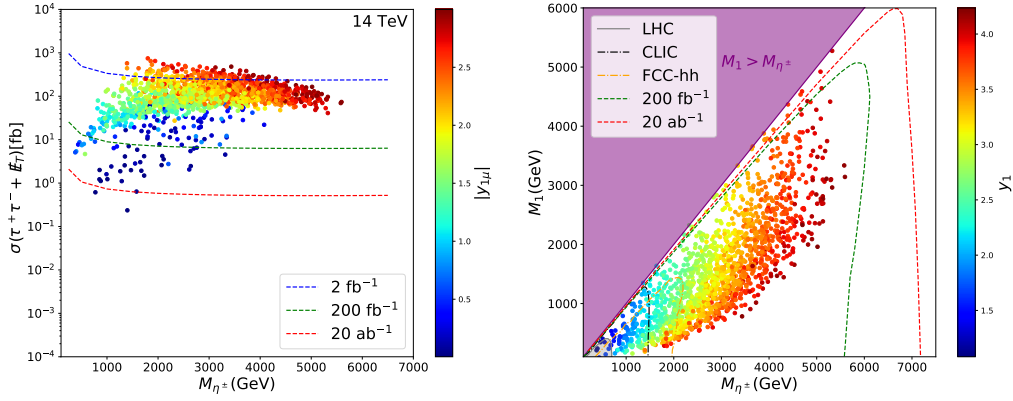


**Figure 10.** Same as Fig. 8, but for the ditau signature.

An efficient cut to suppress the  $\tau^+\tau^-$  channel is

$$|\pi - \theta_{\tau^+} - \theta_{\tau^-}| > 0.04. \quad (5.21)$$

Because the angle resolution of  $\tau$  is worse than that of  $\mu$ , the rejected acollinearity region of the ditau signature is much larger than the dimuon signature region. And the direct ditau events can not be suppressed to a negligible level by the above acollinearity cut. The following cuts in Equation (5.22) and (5.23) are also hard to reject all the  $\tau^+\tau^-$  samples. We then require

$$|\eta_{\tau^\pm}| < 2.5. \quad (5.22)$$

To further suppress the  $\tau^+\tau^-\bar{\nu}_\ell\nu_\ell$  and  $W^+W^-\bar{\nu}_\ell\nu_\ell$  background, the cuts on ditau energy and invariant mass are adopted

$$E_{\tau^+} + E_{\tau^-} > 1 \text{ TeV}, M_{\tau^+\tau^-} > 0.5 \text{ TeV}. \quad (5.23)$$

These two cuts are able to suppress the total background less than 0.1 fb. In the down-right panel of Figure 9, we show the distribution of  $|\vec{P}_{\tau^+} + \vec{P}_{\tau^-}|$  after applying all cuts from Equation (5.19) - (5.23). Comparing with the distribution of  $|\vec{P}_{\mu^+} + \vec{P}_{\mu^-}|$  in Figure 7, the  $\tau^+\tau^-\bar{\nu}_\ell\nu_\ell$  channel does not have any peak structure around 5 TeV. This is because the ditau energy  $E_{\tau^+} + E_{\tau^-}$  is always smaller than 1.5 TeV for the  $\tau^+\tau^-\bar{\nu}_\ell\nu_\ell$  channel as shown in the middle-right panel of Figure 9. Except for the tiny  $\tau^+\tau^-$  channel, both the  $\tau^+\tau^-\bar{\nu}_\ell\nu_\ell$  and  $W^+W^-\bar{\nu}_\ell\nu_\ell$  channel have quite a similar  $|\vec{P}_{\tau^+} + \vec{P}_{\tau^-}|$  distribution as the signal. Therefore, we do not apply any cut on  $|\vec{P}_{\tau^+} + \vec{P}_{\tau^-}|$ .

After the above cuts on the ditau signature, we finally have 2.22 fb, 5.87 fb and 5.36 fb for BP-1 to BP-3. These values are slightly smaller than the corresponding dimuon channel. The total background is 0.062 fb after all cuts. The expected significance would be 20.8 for BP-1, 34.1 for BP-2, and 32.6 for BP-3 with  $200 \text{ fb}^{-1}$  luminosity. For BP-2 and BP-3,  $5 \text{ fb}^{-1}$  data is able to reach the  $5\sigma$  discovery limit. Meanwhile, we need  $11.6 \text{ fb}^{-1}$  data to discover BP-1.

$\sigma(\text{fb})$	<b>BP-1</b>	<b>BP-2</b>	<b>BP-3</b>	$\gamma\bar{\nu}_\ell\nu_\ell$
Preselection	2.76	15.99	18.91	3277
$0.70 < \theta_\gamma < 2.44$	1.19	7.09	8.47	1399
$E_\gamma > 500 \text{ GeV}$	0.55	2.86	3.00	54.19
$\cancel{E}_T > 1 \text{ TeV}$	0.39	1.82	1.72	10.96
$P_T^\gamma > 2 \text{ TeV}$	0.27	1.07	0.84	2.23
Significance	2.41	8.33	6.78	
$5\sigma$ Luminosity ( $\text{fb}^{-1}$ )	857	72	109	

**Table 4.** Cut flow table for the mono-photon signature  $\gamma + \cancel{E}_T$  from BP-1, BP-2, BP-3 and the dominant background  $\gamma\bar{\nu}_\ell\nu_\ell$ .

In Figure 10, the  $5\sigma$  discovery reaches of the two specific scenarios for the ditau signature are shown. In the left panel, the theoretical ditau cross-section is calculated as

$$\sigma(\tau^+\tau^- + \cancel{E}_T) = \sigma(\eta^+\eta^-) \times \text{BR}_{\tau N_1}^2. \quad (5.24)$$

Different from the dimuon signature, the branching ratio of  $\tau$  final state is never suppressed. So the ditau cross-section is always larger than 0.1 fb. Provided  $M_1 = M_{\eta^\pm}/2$ , we then obtain the total cut efficiency is approximately 0.05 for the signal. For the most promising case, the 14 TeV MuC is able to probe  $\sigma(\tau^+\tau^- + \cancel{E}_T) \gtrsim 250 \text{ fb}$  in the range of  $M_{\eta^\pm} \in [1.5, 4] \text{ TeV}$  with only  $2 \text{ fb}^{-1}$  data. Samples with  $\sigma(\tau^+\tau^- + \cancel{E}_T) \gtrsim 6.5 \text{ fb}$  are within the reach of  $200 \text{ fb}^{-1}$ . This covers most samples with  $|y_{1\mu}| \gtrsim 1$ . By increasing the integrated luminosity to  $20 \text{ ab}^{-1}$ , the  $5\sigma$  discovery limit is down to about 0.5 fb, which unravels almost all samples.

In the right panel of Figure 10, the  $5\sigma$  discovery limits on the  $M_{\eta^\pm} - M_1$  plane with  $y_{1e} = 0.02, y_{1\mu} = y_{1\tau} = 2$  are shown. With lower tagging efficiency for the ditau system, we find that the significance of this channel at best could reach  $4.9\sigma$  with  $2 \text{ fb}^{-1}$  data, so there is no corresponding  $5\sigma$  discovery reach for  $2 \text{ fb}^{-1}$  in the plot. With  $200 \text{ fb}^{-1}$  data, the ditau channel could discover the region with  $M_{\eta^\pm} \lesssim 6.1 \text{ TeV}$  and  $M_1 \lesssim 5.1 \text{ TeV}$ . Although this region is smaller than the dimuon channel with same luminosity, it is enough to cover most allowed samples. Similarly, the compressed mass region can be hardly probe by the ditau channel even with  $20 \text{ ab}^{-1}$  data either.

### 5.3 Mono- $\gamma$ Signature

Another interesting channel is the mono-photon signature  $\mu^+\mu^- \rightarrow N_1 N_1 \gamma \rightarrow \gamma + \cancel{E}_T$  [101], with the photon from initial state radiation [102]. This signature is mediated by the  $t$ -channel exchange of  $\eta^\pm$ , thus the cross-section is also enhanced by relatively large  $|y_{1\mu}|$ . The dominant background is from  $\gamma\bar{\nu}_\ell\nu_\ell$  [103].

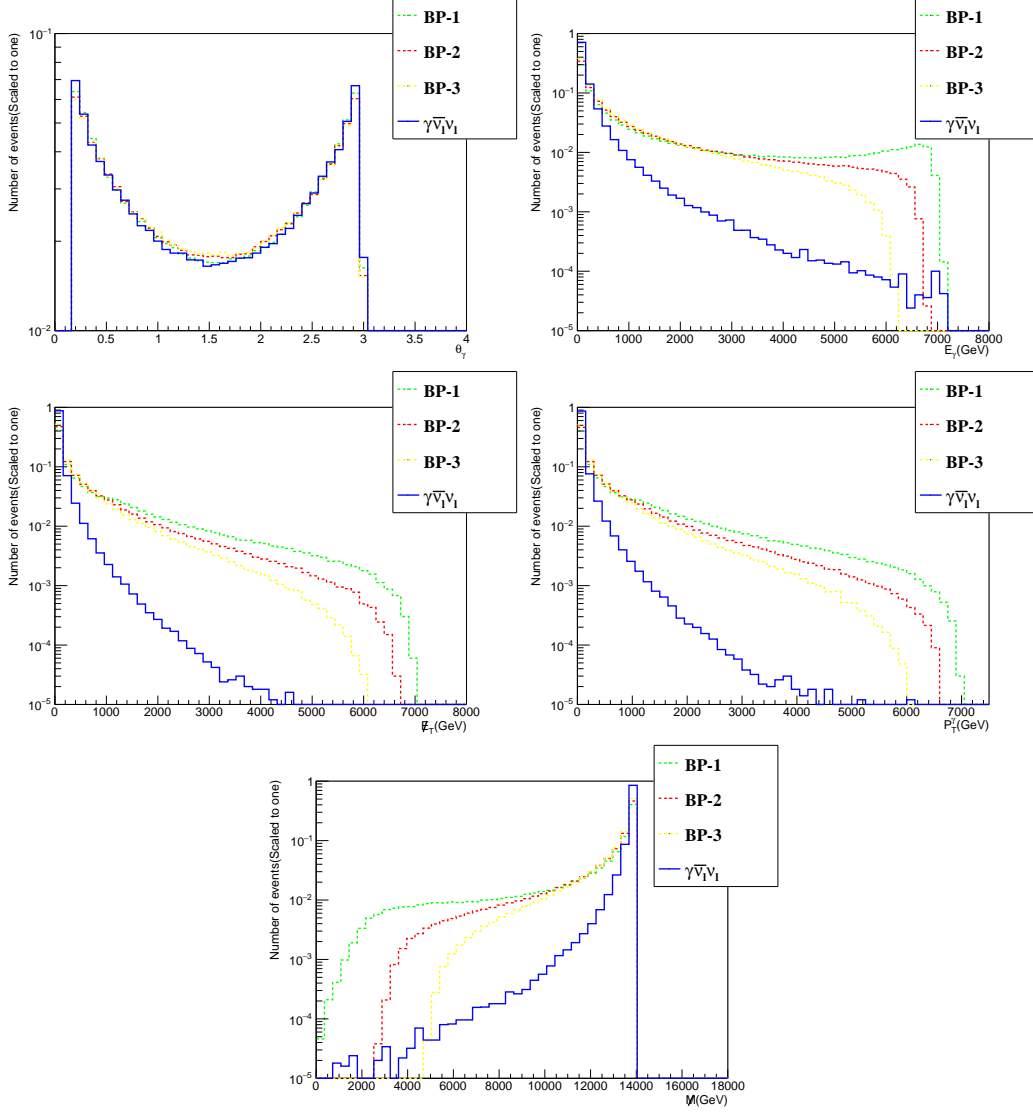


**Figure 11.** Normalized distributions of the  $\theta$  angle of photon  $\theta_\gamma$  (up-left panel), energy of the photon  $E_\gamma$  (up-right panel), missing transverse energy  $\cancel{E}_T$  (middle-left panel), transverse momentum of the photon  $P_T^\gamma$  (middle-right panel), and missing mass  $\mathcal{M}$  (down panel).

The initial cross-section of the benchmark points are typically at the order of  $\mathcal{O}(10)$  fb, while the cross-section of background is two orders of magnitudes higher. In Figure 11, the normalized distribution of relevant parameters are shown. The missing mass  $\mathcal{M}$  is defined as [45]

$$\mathcal{M} = \sqrt{(p_{\mu^+} + p_{\mu^-} - \sum_i p_i)^2}, \quad (5.25)$$

where  $p_{\mu^\pm}$  is the momenta of initial muon and  $p_i$  is the momenta of the  $i$ -th observed particles in the final states. From the distribution of missing mass  $\mathcal{M}$  in Figure 11, it is obvious that the signals predict  $\mathcal{M} > 2M_1$ . However, applying the cut  $\mathcal{M} > 2M_1$  only

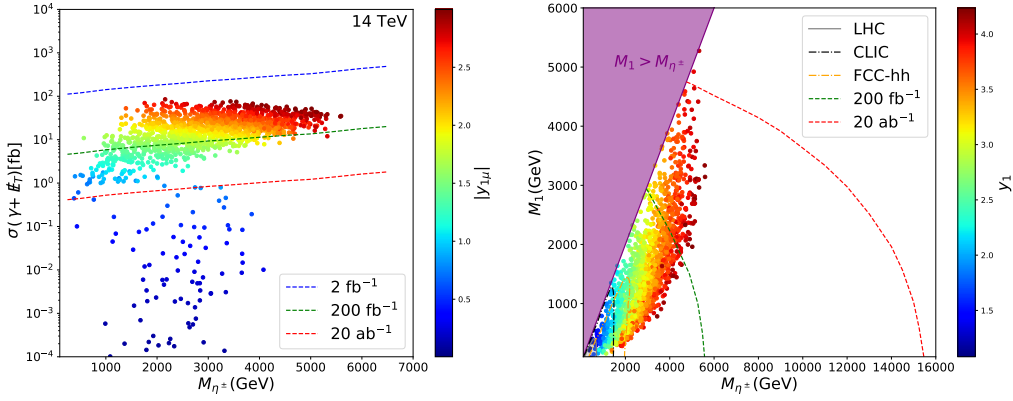


**Figure 12.** Same as Fig. 8, but for the mono-photon signature.

rejects very small amount of the background. So we do not apply cut on  $\mathcal{M}$ .

Following Ref. [103], we first select events with

$$0.69 < \theta_\gamma < 2.44. \quad (5.26)$$

At this level of cut, the background  $\gamma\bar{\nu}_\ell\nu_\ell$  is still at the order of  $\mathcal{O}(10^3)$  fb. From the distribution of  $E_\gamma$ , it is clear the signals have relatively larger values than the background. The same is true for the distributions of  $\cancel{E}_T$  and  $P_T^\gamma$ . We then apply the following cuts

$$E_\gamma > 500 \text{ GeV}, \cancel{E}_T > 1 \text{ TeV}, P_T^\gamma > 2 \text{ TeV}. \quad (5.27)$$

The above cuts are much tighter than those in Ref. [103], but they are efficient to suppress the background. After the cuts in Equation (5.27), the cross-section of the signal and background are comparable.

The cut flow for the mono-photon signature and background are summarized in Table 4. The final cross-sections of signals are 0.27 fb, 1.07 fb, and 0.84 fb for BP-1, BP-2, and BP-3, respectively. The final cross-section of background is 2.23 fb. Provided an integrated luminosity of  $200 \text{ fb}^{-1}$ , the expected significance will reach 2.41 for BP-1, 8.33 for BP-2, and 6.78 for BP-3. To reach the  $5\sigma$  discovery limit, the required luminosity is  $857 \text{ fb}^{-1}$  for BP-1,  $72 \text{ fb}^{-1}$  for BP-2, and  $109 \text{ fb}^{-1}$  for BP-3. Comparing with the dilepton signature, this mono-photon signature is less promising.

In Figure 12, the  $5\sigma$  discovery reaches of the two specific scenarios for the mono-photon signature are shown. In the left panel, the theoretical mono-photon cross-section is calculated by **MadGraph5\_aMC@NLO** [98]. The predicted mono-photon cross-section is less than 80 fb. With the cuts shown in Table 4, the cut efficiency for the scenario  $M_1 = M_{\eta^\pm}/2$  decreases from 0.12 to 0.03 when  $M_{\eta^\pm}$  increases. According to our simulation, no samples are within the reach of  $2 \text{ fb}^{-1}$  data. Provided an integrated luminosity of  $200 \text{ fb}^{-1}$ , the 14 TeV MuC could discover the samples with  $\sigma(\gamma + \cancel{E}_T) \gtrsim 10 \text{ fb}$ , which corresponds to  $|y_{1\mu}| \gtrsim 1.5$ . The final  $20 \text{ ab}^{-1}$  data would push the  $5\sigma$  discovery limit down to about 1 fb, but is still hard to probe the  $|y_{1\mu}| \lesssim 1$  region in this mono-photon channel.

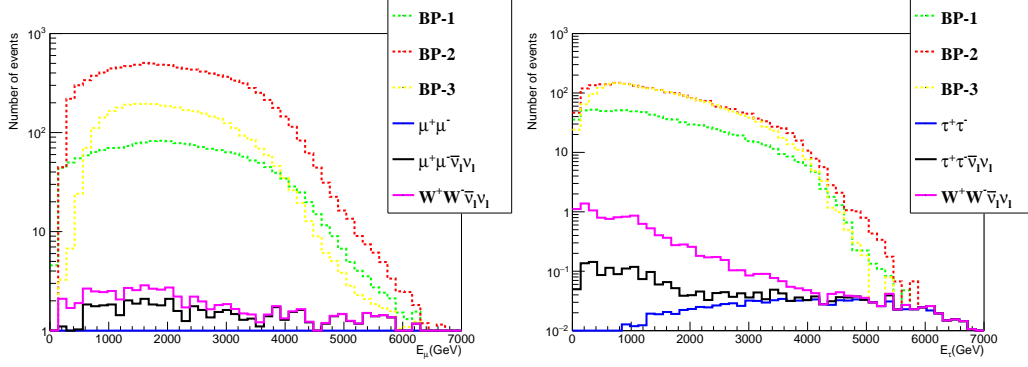


**Figure 13.** Distribution of the lepton energy  $E_\mu$  (left) and  $E_\tau$  (right) after applying all cuts. Here, we assume an integrated luminosity of  $200 \text{ fb}^{-1}$ .

Fixing  $y_{1e} = 0.02, y_{1\mu} = y_{1\tau} = 2$ , the  $5\sigma$  discovery limits on the  $M_{\eta^\pm} - M_1$  plane are shown in the right panel of Figure 12. We do not find the corresponding  $5\sigma$  discovery limit for  $2 \text{ fb}^{-1}$  in this analysis. The region with  $M_1 \lesssim 3 \text{ TeV}$  and  $M_{\eta^\pm} \lesssim 5.5 \text{ TeV}$  is unrevealed by  $200 \text{ fb}^{-1}$  data. Increasing the luminosity to  $20 \text{ ab}^{-1}$  is able to cover almost all samples. Notably, the mono-photon signature is also sensitive to the compressed mass region  $M_1 \simeq M_{\eta^\pm}$ . For  $M_{\eta^\pm}$  above  $7 \text{ TeV}$ , the mono-photon signature can also reach  $5\sigma$  when  $M_1 \lesssim 4 \text{ TeV}$  with  $20 \text{ ab}^{-1}$  data. So this signal is expected powerful to probe the heavy  $\eta^\pm$  region at lower collision energy, e.g., a  $6 \text{ TeV}$  MuC.

#### 5.4 Mass Measurement

At MuC, masses of charged scalar  $\eta^\pm$  and dark matter  $N_1$  can be extracted from the endpoints of the lepton energy distribution [73, 104]

$$M_{\eta^\pm} = \sqrt{s} \frac{\sqrt{E_L E_H}}{E_L + E_H}, \quad M_1 = M_{\eta^\pm} \left( 1 - \frac{2(E_H + E_L)}{\sqrt{s}} \right)^{1/2}, \quad (5.28)$$

with the higher and lower endpoints  $E_{H,L}$  given by

$$E_{H,L} = \frac{\sqrt{s}}{4} \left( 1 - \frac{M_1^2}{M_{\eta^\pm}^2} \right) \left( 1 \pm \sqrt{1 - 4 \frac{M_{\eta^\pm}^2}{s}} \right). \quad (5.29)$$

For example, BP-2 predicts the higher and lower endpoints to be  $E_H = 4342 \text{ GeV}$  and  $E_L = 167 \text{ GeV}$ .

The backgrounds should be suppressed to tiny level in order to observe these two endpoints. In Figure 13, we show the distribution of  $E_\mu$  and  $E_\tau$  after applying all cuts. Compared with the signal, the backgrounds are small enough. However, the endpoints of the signals are not always so clear to obtain. The lower endpoints in the distribution of  $E_\mu$  are clear, but are smeared in the distribution of  $E_\tau$ . Meanwhile, the higher endpoints in the distributions actually correspond to knee structures.

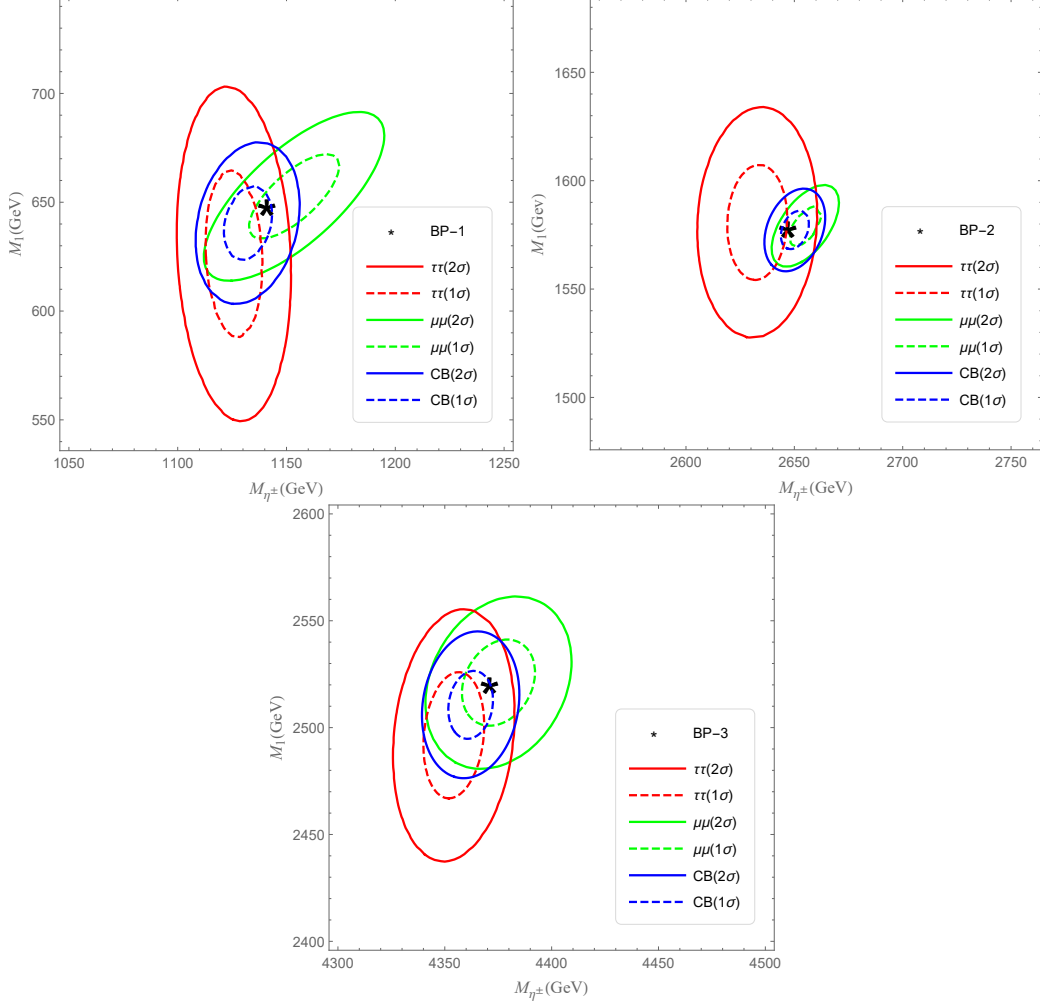


**Figure 14.** The fitted results of the benchmark points in the  $M_{\eta^\pm} - M_1$  plane for both  $\mu^+\mu^- + \cancel{E}_T$  and  $\tau^+\tau^- + \cancel{E}_T$  channel. Here, we assume an integrated luminosity of  $200 \text{ fb}^{-1}$ . The red and green lines are the results of  $\tau^+\tau^- + \cancel{E}_T$  and  $\mu^+\mu^- + \cancel{E}_T$  channel. The blue lines are the combined (denoted as CB) results of the dimuon and ditau channel. The dashed and solid lines correspond to the  $1\sigma$  and  $2\sigma$  range. The stars  $\star$  are the actual values for the benchmark points.

To further determine the masses of charged scalar  $\eta^\pm$  and DM  $N_1$ , we then perform a binned likelihood fit. The logarithm of the likelihood is defined as [104]

$$\log \mathcal{L}(M_{\eta^\pm}, M_1) = \sum_i^{n_b} A_i(M_{\eta^\pm}, M_1) \log B_i - B_i, \quad (5.30)$$

where  $n_b$  is the number of bins,  $A_i(M_{\eta^\pm}, M_1)$  is the expected number of events in the  $i$ -th bin with masses  $M_{\eta^\pm}$  and  $M_1$ ,  $B_i$  is the measured number of events in the  $i$ -th bin. During our simulation, we set  $B_i$  to be the event number predicted by the benchmark points and corresponding backgrounds.

The fitted results are shown in Figure 14. Generally speaking, the actual values of

	BP-1		BP-2		BP-3	
	$M_{\eta^\pm}$	$M_1$	$M_{\eta^\pm}$	$M_1$	$M_{\eta^\pm}$	$M_1$
Actual Value	1141	648.7	2647	1579	4371	2521
$\mu^+\mu^- + \cancel{E}_T$	$1153 \pm 20$	$653 \pm 19$	$2655 \pm 7$	$1579 \pm 9$	$4375 \pm 16$	$2521 \pm 19$
$\tau^+\tau^- + \cancel{E}_T$	$1126 \pm 13$	$626 \pm 38$	$2633 \pm 14$	$1581 \pm 26$	$4354 \pm 14$	$2496 \pm 29$
Combined	$1132 \pm 11$	$640 \pm 17$	$2650 \pm 7$	$1577 \pm 9$	$4362 \pm 10$	$2511 \pm 16$

**Table 5.** The actual values of benchmark points and corresponding fitted results for dimuon, ditau and combined channel. All the masses are in the unit of GeV.

benchmark points are within the  $2\sigma$  range of the dimuon and ditau results. With a larger cross-section after all cuts, the dimuon channel usually has a better mass resolution than the ditau channel. We also find that the best fit values for  $M_{\eta^\pm}$  of the dimuon channel are always larger than those of the ditau channel. There are strong correlations between  $M_{\eta^\pm}$  and  $M_1$  in the dimuon channel for all three benchmark points. After combining the results of the dimuon and ditau channel, the true values of benchmark points are within the  $1\sigma$  range of the fitted results.

In Table 5, we summarize the fitted results for the dimuon, ditau and combined channel. For BP-1 and BP-3, the actual values are in the  $1\sigma$  range of the dimuon channel, but are out the  $1\sigma$  range of the ditau channel. For BP-2, the dimuon channel is the most precise one due to the largest cross-section after all cuts. The actual value of BP-2 is on the edges of  $1\sigma$  range for both dimuon and ditau channel. The combined results indicate that masses of charged scalar  $\eta^\pm$  and dark matter  $N_1$  can be measured at the level of  $\mathcal{O}(10)$  GeV with  $200 \text{ fb}^{-1}$  data.

Besides the lepton energy distribution, masses of the dark sector can be reconstructed by other variables separately. One is the missing mass  $\mathcal{M}$  defined in Equation (5.25), which in theory predicts  $\mathcal{M} > 2M_1$  for the signal. Another one is the  $M_{T2}$  variable defined as [105, 106],

$$M_{T2} = \min_{\mathbf{q}_{T,1} + \mathbf{q}_{T,2} = \cancel{E}_T} \left\{ \max \left[ M_T(\mathbf{P}_T^{l_1}, \mathbf{q}_{T,1}), M_T(\mathbf{P}_T^{l_2}, \mathbf{q}_{T,2}) \right] \right\}, \quad (5.31)$$

where  $\mathbf{P}_T^{l_1}$  and  $\mathbf{P}_T^{l_2}$  are the transverse momentum vectors of the two leptons,  $\mathbf{q}_{T,1}$  and  $\mathbf{q}_{T,2}$  are all possible combinations of two transverse momentum vectors that satisfy  $\mathbf{q}_{T,1} + \mathbf{q}_{T,2} = \cancel{E}_T$ . The  $M_{T2}$  variable predicts  $M_{T2} < M_{\eta^\pm}$  for the signal.

In Figure 15, we show the events number of  $\mathcal{M}$  and  $M_{T2}$  after applying all selection cuts in the dilepton and mono-photon signature. In the dimuon and ditau signature, the distribution of  $\mathcal{M}$  is affected by the applied cuts. In the mono-photon signature, although the lower edges of benchmark points are clear with the signal only, the relatively large background makes it hard to directly observe them. As for the variable  $M_{T2}$ , the upper edges of benchmark points are obvious. Therefore, we may extract the mass of dark matter

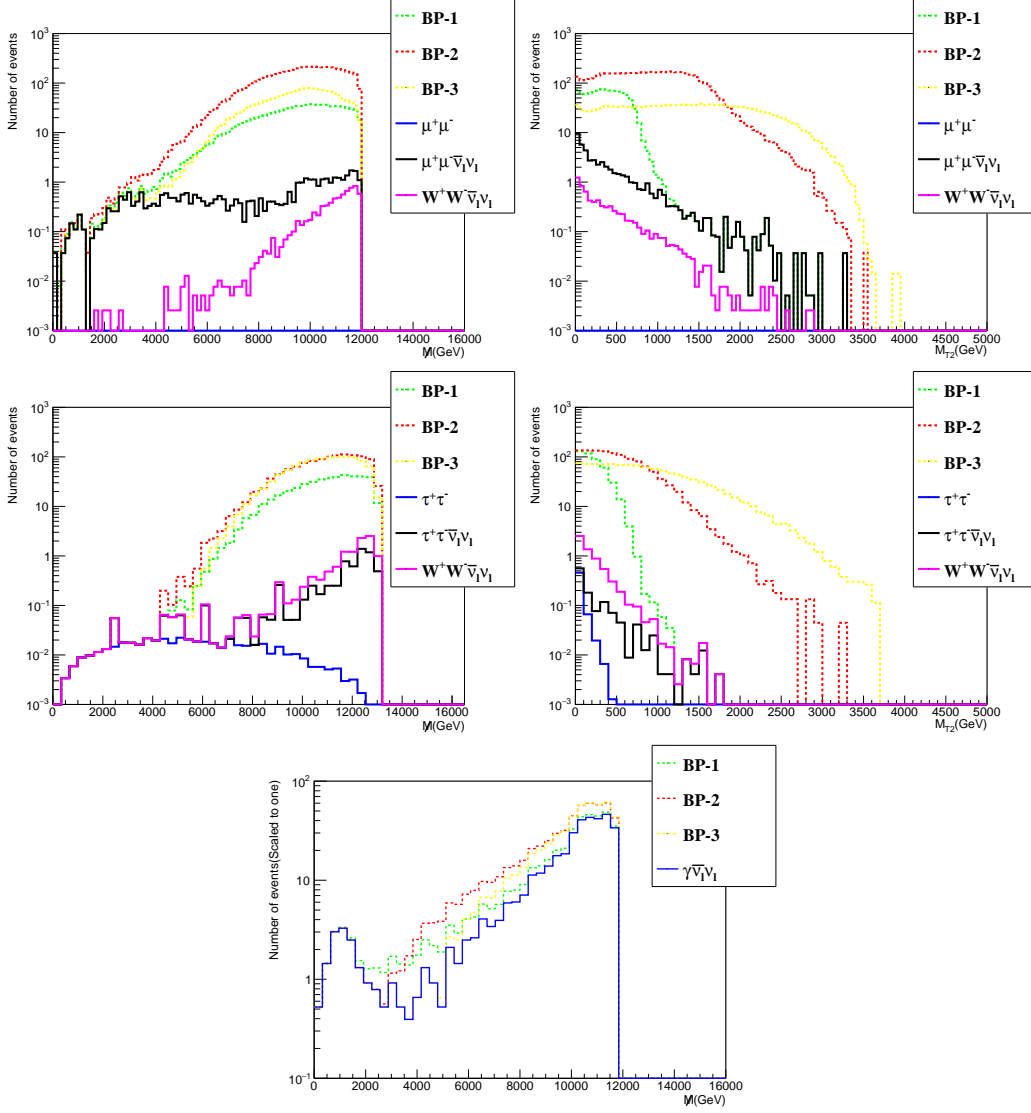


**Figure 15.** Events number of  $\mathcal{M}$  and  $M_{T2}$  in the dilepton and mono-photon signature after applying all cuts with  $200 \text{ fb}^{-1}$  data.

$N_1$  from  $\mathcal{M}$  in the mono-photon signal and mass of charged scalar  $\eta^\pm$  from  $M_{T2}$  in the dilepton signal separately by performing binned likelihood fits.

## 6 Conclusion

The Scotogenic model is an appealing way to explain the origin of tiny neutrino mass and dark matter. Three singlet fermion  $N_i$  and one inert doublet scalar  $\eta$  are introduced in this model. In this paper, we consider the lightest singlet fermion  $N_1$  as dark matter. Under the tight constraints from LFV and relic density, a hierarchical Yukawa structure  $|y_{1e}| \ll |y_{1\mu}| \sim |y_{1\tau}| \sim \mathcal{O}(1)$  is usually favored. With large  $\mu$ -related Yukawa coupling,

the cross-section of charged scalar  $\eta^\pm$  at MuC is greatly enhanced, which leads to the MuC as an ideal machine to probe the Scotogenic model. In this paper, we investigate the dilepton and mono-photon signature of the Scotogenic model at a 14 TeV MuC.

The most promising channel is the dimuon signature produced via  $\mu^+\mu^- \rightarrow \eta^+\eta^- \rightarrow \mu^+N_1 + \mu^-N_1 \rightarrow \mu^+\mu^- + \cancel{E}_T$ . According to our simulation, only  $1 \text{ fb}^{-1}$  data is enough to reach the  $5\sigma$  discovery reach for BP-2 ( $M_{\eta^\pm} = 2647 \text{ GeV}$ ,  $M_1 = 1579 \text{ GeV}$ ,  $|y_{1\mu}| = 1.99$ ). With  $200 \text{ fb}^{-1}$  data, the 14 TeV MuC is able to unravel most viable samples, except those with small Yukawa coupling  $|y_{1\mu}|$  or with compressed mass spectrum  $M_1 \simeq M_{\eta^\pm}$ . The compressed mass region is even hard to probe by the cuts in our analysis even with  $20 \text{ ab}^{-1}$  data. For the ditau signature produced via  $\mu^+\mu^- \rightarrow \eta^+\eta^- \rightarrow \tau^+N_1 + \tau^-N_1 \rightarrow \tau^+\tau^- + \cancel{E}_T$ , it is usually less promising than the dimuon channel. To obtain  $5\sigma$  discovery, we need about  $4.3 \text{ fb}^{-1}$  data for BP-2. But when  $|y_{1\mu}|$  is too small, the ditau channel becomes more promising. Almost all the samples are within the reach of  $20 \text{ ab}^{-1}$  data for the ditau channel. The mono-photon signature is produced via  $\mu^+\mu^- \rightarrow \gamma N_1 N_1 \rightarrow \gamma + \cancel{E}_T$  by the  $t$ -channel exchange of  $\eta^\pm$ . The mono-photon signal is promising with  $|y_{1\mu}| \gtrsim 1$ . As for the compressed mass region, the mono-photon signature is also able to reach  $5\sigma$  significance with  $20 \text{ ab}^{-1}$  for  $M_1 \lesssim 5 \text{ TeV}$ . At MuC, masses of the charged scalar  $\eta^\pm$  and dark matter  $N_1$  can be further measured by fitting of the distribution of lepton energy. For instance, the fitted results of BP-2 are  $M_{\eta^\pm} = 2655 \pm 7 \text{ GeV}$  with  $M_1 = 1579 \pm 9 \text{ GeV}$  in the dimuon channel and  $M_{\eta^\pm} = 2633 \pm 14 \text{ GeV}$  with  $M_1 = 1581 \pm 26 \text{ GeV}$  in the ditau channel. The combined result is  $M_{\eta^\pm} = 2650 \pm 7 \text{ GeV}$  with  $M_1 = 1577 \pm 9 \text{ GeV}$  allowing the actual value within the  $1\sigma$  range.

Besides the dilepton and mono-photon signature discussed in this paper, we highlight some other interesting signals. With a compressed mass spectrum  $M_1 \simeq M_{\eta^\pm}$ , the calculation of dark matter relic density should be improved by including the coannihilation effect [37]. As already shown in Figure 8 and 10, the leptons from  $\eta^\pm \rightarrow \ell^\pm N_1$  decays in this scenario are relatively soft, thus are hard to detect with the cuts in this paper. Searches for the compressed mass region need the *LowPt* criterion [40], which is beyond the scope of this work. In this paper, we only consider the same flavor dilepton signature. The different flavor dilepton signatures as  $\mu^\pm\tau^\mp + \cancel{E}_T$ ,  $\tau^\pm e^\mp + \cancel{E}_T$  and  $\mu^\pm e^\mp + \cancel{E}_T$  are also possible. Meanwhile, if the heavier singlet fermions  $N_j (j = 2, 3)$  are light enough, they can be singly and doubly produced at MuC via  $\mu^+\mu^- \rightarrow N_j N_1, N_j N_j$ . Then the cascade decay  $N_j \rightarrow \ell^\pm \eta^\mp \rightarrow \ell^\pm \ell^\mp N_1$  will lead to dilepton and tetra-lepton signature. Studies of these signatures will further enlighten the nature of Scotogenic model.

## Acknowledgments

This work is supported by the National Natural Science Foundation of China under Grant No. 11805081 and 11635009, Natural Science Foundation of Shandong Province under Grant No. ZR2019QA021, the Open Project of Guangxi Key Laboratory of Nuclear Physics and Nuclear Technology under Grant No. NLK2021-07.

## References

- [1] L. M. Krauss, S. Nasri and M. Trodden, *A Model for neutrino masses and dark matter*, *Phys. Rev. D* **67** (2003) 085002 [[hep-ph/0210389](#)].
- [2] T. Asaka, S. Blanchet and M. Shaposhnikov, *The nuMSM, dark matter and neutrino masses*, *Phys. Lett. B* **631** (2005) 151 [[hep-ph/0503065](#)].
- [3] E. Ma, *Verifiable radiative seesaw mechanism of neutrino mass and dark matter*, *Phys. Rev. D* **73** (2006) 077301 [[hep-ph/0601225](#)].
- [4] M. Aoki, S. Kanemura and O. Seto, *Neutrino mass, Dark Matter and Baryon Asymmetry via TeV-Scale Physics without Fine-Tuning*, *Phys. Rev. Lett.* **102** (2009) 051805 [[0807.0361](#)].
- [5] D. Restrepo, O. Zapata and C. E. Yaguna, *Models with radiative neutrino masses and viable dark matter candidates*, *JHEP* **11** (2013) 011 [[1308.3655](#)].
- [6] M. Escudero, N. Rius and V. Sanz, *Sterile Neutrino portal to Dark Matter II: Exact Dark symmetry*, *Eur. Phys. J. C* **77** (2017) 397 [[1607.02373](#)].
- [7] Y. Cai, J. Herrero-García, M. A. Schmidt, A. Vicente and R. R. Volkas, *From the trees to the forest: a review of radiative neutrino mass models*, *Front. in Phys.* **5** (2017) 63 [[1706.08524](#)].
- [8] G. Cacciapaglia and M. Rosenlyst, *Loop-generated neutrino masses in composite Higgs models*, *JHEP* **09** (2021) 167 [[2010.01437](#)].
- [9] J. Kubo, E. Ma and D. Suematsu, *Cold Dark Matter, Radiative Neutrino Mass,  $\mu \rightarrow e\gamma$ , and Neutrinoless Double Beta Decay*, *Phys. Lett. B* **642** (2006) 18 [[hep-ph/0604114](#)].
- [10] D. Aristizabal Sierra, J. Kubo, D. Restrepo, D. Suematsu and O. Zapata, *Radiative seesaw: Warm dark matter, collider and lepton flavour violating signals*, *Phys. Rev. D* **79** (2009) 013011 [[0808.3340](#)].
- [11] D. Suematsu, T. Toma and T. Yoshida, *Reconciliation of CDM abundance and  $\mu \rightarrow e\gamma$  in a radiative seesaw model*, *Phys. Rev. D* **79** (2009) 093004 [[0903.0287](#)].
- [12] S. Kanemura, O. Seto and T. Shimomura, *Masses of dark matter and neutrino from TeV scale spontaneous  $U(1)_{B-L}$  breaking*, *Phys. Rev. D* **84** (2011) 016004 [[1101.5713](#)].
- [13] D. Schmidt, T. Schwetz and T. Toma, *Direct Detection of Leptophilic Dark Matter in a Model with Radiative Neutrino Masses*, *Phys. Rev. D* **85** (2012) 073009 [[1201.0906](#)].
- [14] S. Baek, H. Okada and K. Yagyu, *Flavour Dependent Gauged Radiative Neutrino Mass Model*, *JHEP* **04** (2015) 049 [[1501.01530](#)].
- [15] A. Merle and M. Platscher, *Parity Problem of the Scotogenic Neutrino Model*, *Phys. Rev. D* **92** (2015) 095002 [[1502.03098](#)].
- [16] A. Ahriche, A. Jueid and S. Nasri, *Radiative neutrino mass and Majorana dark matter within an inert Higgs doublet model*, *Phys. Rev. D* **97** (2018) 095012 [[1710.03824](#)].

- [17] T. Hugle, M. Platscher and K. Schmitz, *Low-Scale Leptogenesis in the Scotogenic Neutrino Mass Model*, *Phys. Rev. D* **98** (2018) 023020 [[1804.09660](#)].
- [18] S. Baumholzer, V. Brdar and P. Schwaller, *The New  $\nu$ MSM ( $\nu\nu$ MSM): Radiative Neutrino Masses, keV-Scale Dark Matter and Viable Leptogenesis with sub-TeV New Physics*, *JHEP* **08** (2018) 067 [[1806.06864](#)].
- [19] A. Ahriche, A. Arhrib, A. Jueid, S. Nasri and A. de La Puente, *Mono-Higgs Signature in the Scotogenic Model with Majorana Dark Matter*, *Phys. Rev. D* **101** (2020) 035038 [[1811.00490](#)].
- [20] Z.-L. Han and W. Wang, *Predictive Scotogenic Model with Flavor Dependent Symmetry*, *Eur. Phys. J. C* **79** (2019) 522 [[1901.07798](#)].
- [21] W. Wang and Z.-L. Han,  *$U(1)_{B-3L_\alpha}$  extended scotogenic models and single-zero textures of neutrino mass matrices*, *Phys. Rev. D* **101** (2020) 115040 [[1911.00819](#)].
- [22] D. Borah, A. Dasgupta, K. Fujikura, S. K. Kang and D. Mahanta, *Observable Gravitational Waves in Minimal Scotogenic Model*, *JCAP* **08** (2020) 046 [[2003.02276](#)].
- [23] Y. Liao and X.-D. Ma, *One-loop Matching of Scotogenic Model onto Standard Model Effective Field Theory up to Dimension 7*, [2210.04270](#).
- [24] E. M. Dolle and S. Su, *The Inert Dark Matter*, *Phys. Rev. D* **80** (2009) 055012 [[0906.1609](#)].
- [25] A. Arhrib, Y.-L. S. Tsai, Q. Yuan and T.-C. Yuan, *An Updated Analysis of Inert Higgs Doublet Model in light of the Recent Results from LUX, PLANCK, AMS-02 and LHC*, *JCAP* **06** (2014) 030 [[1310.0358](#)].
- [26] A. Belyaev, G. Cacciapaglia, I. P. Ivanov, F. Rojas-Abatte and M. Thomas, *Anatomy of the Inert Two Higgs Doublet Model in the light of the LHC and non-LHC Dark Matter Searches*, *Phys. Rev. D* **97** (2018) 035011 [[1612.00511](#)].
- [27] F. S. Queiroz and C. E. Yaguna, *The CTA aims at the Inert Doublet Model*, *JCAP* **02** (2016) 038 [[1511.05967](#)].
- [28] C. Garcia-Cely, M. Gustafsson and A. Ibarra, *Probing the Inert Doublet Dark Matter Model with Cherenkov Telescopes*, *JCAP* **02** (2016) 043 [[1512.02801](#)].
- [29] B. Eiteneuer, A. Goudelis and J. Heisig, *The inert doublet model in the light of Fermi-LAT gamma-ray data: a global fit analysis*, *Eur. Phys. J. C* **77** (2017) 624 [[1705.01458](#)].
- [30] E. Dolle, X. Miao, S. Su and B. Thomas, *Dilepton Signals in the Inert Doublet Model*, *Phys. Rev. D* **81** (2010) 035003 [[0909.3094](#)].
- [31] X. Miao, S. Su and B. Thomas, *Trilepton Signals in the Inert Doublet Model*, *Phys. Rev. D* **82** (2010) 035009 [[1005.0090](#)].
- [32] J. Kalinowski, W. Kotlarski, T. Robens, D. Sokolowska and A. F. Zarnecki, *Exploring Inert Scalars at CLIC*, *JHEP* **07** (2019) 053 [[1811.06952](#)].
- [33] F.-X. Yang, Z.-L. Han and Y. Jin, *Same-Sign Dilepton Signature in the Inert Doublet Model*, *Chin. Phys. C* **45** (2021) 073114 [[2101.06862](#)].

- [34] Y.-Z. Fan, T.-P. Tang, Y.-L. S. Tsai and L. Wu, *Inert Higgs Dark Matter for CDF II W-Boson Mass and Detection Prospects*, *Phys. Rev. Lett.* **129** (2022) 091802 [2204.03693].
- [35] A. Ibarra, C. E. Yaguna and O. Zapata, *Direct Detection of Fermion Dark Matter in the Radiative Seesaw Model*, *Phys. Rev. D* **93** (2016) 035012 [1601.01163].
- [36] T. Toma and A. Vicente, *Lepton Flavor Violation in the Scotogenic Model*, *JHEP* **01** (2014) 160 [1312.2840].
- [37] A. Vicente and C. E. Yaguna, *Probing the scotogenic model with lepton flavor violating processes*, *JHEP* **02** (2015) 144 [1412.2545].
- [38] S. Baumholzer, V. Brdar, P. Schwaller and A. Segner, *Shining Light on the Scotogenic Model: Interplay of Colliders and Cosmology*, *JHEP* **09** (2020) 136 [1912.08215].
- [39] ATLAS collaboration, G. Aad et al., *Search for electroweak production of charginos and sleptons decaying into final states with two leptons and missing transverse momentum in  $\sqrt{s} = 13$  TeV pp collisions using the ATLAS detector*, *Eur. Phys. J. C* **80** (2020) 123 [1908.08215].
- [40] ATLAS collaboration, G. Aad et al., *Searches for electroweak production of supersymmetric particles with compressed mass spectra in  $\sqrt{s} = 13$  TeV pp collisions with the ATLAS detector*, *Phys. Rev. D* **101** (2020) 052005 [1911.12606].
- [41] CMS collaboration, A. M. Sirunyan et al., *Search for supersymmetry in final states with two oppositely charged same-flavor leptons and missing transverse momentum in proton-proton collisions at  $\sqrt{s} = 13$  TeV*, *JHEP* **04** (2021) 123 [2012.08600].
- [42] J. P. Delahaye, M. Diemoz, K. Long, B. Mansoulié, N. Pastrone, L. Rivkin et al., *Muon Colliders*, 1901.06150.
- [43] K. Long, D. Lucchesi, M. Palmer, N. Pastrone, D. Schulte and V. Shiltsev, *Muon colliders to expand frontiers of particle physics*, *Nature Phys.* **17** (2021) 289 [2007.15684].
- [44] T. Han, D. Liu, I. Low and X. Wang, *Electroweak couplings of the Higgs boson at a multi-TeV muon collider*, *Phys. Rev. D* **103** (2021) 013002 [2008.12204].
- [45] T. Han, Z. Liu, L.-T. Wang and X. Wang, *WIMPs at High Energy Muon Colliders*, *Phys. Rev. D* **103** (2021) 075004 [2009.11287].
- [46] W. Liu and K.-P. Xie, *Probing electroweak phase transition with multi-TeV muon colliders and gravitational waves*, *JHEP* **04** (2021) 015 [2101.10469].
- [47] T. Han, S. Li, S. Su, W. Su and Y. Wu, *Heavy Higgs bosons in 2HDM at a muon collider*, *Phys. Rev. D* **104** (2021) 055029 [2102.08386].
- [48] H. Al Ali et al., *The muon Smasher's guide*, *Rept. Prog. Phys.* **85** (2022) 084201 [2103.14043].
- [49] R. Franceschini and M. Greco, *Higgs and BSM Physics at the Future Muon Collider*, *Symmetry* **13** (2021) 851 [2104.05770].

- [50] X.-H. Bai, Z.-L. Han, Y. Jin, H.-L. Li and Z.-X. Meng, *Same-sign tetralepton signature in type-II seesaw at lepton colliders* \*, *Chin. Phys. C* **46** (2022) 012001 [2105.02474].
- [51] S. Bottaro, D. Buttazzo, M. Costa, R. Franceschini, P. Panci, D. Redigolo et al., *Closing the window on WIMP Dark Matter*, *Eur. Phys. J. C* **82** (2022) 31 [2107.09688].
- [52] J. Chen, T. Li, C.-T. Lu, Y. Wu and C.-Y. Yao, *Measurement of Higgs boson self-couplings through  $2 \rightarrow 3$  vector bosons scattering in future muon colliders*, *Phys. Rev. D* **105** (2022) 053009 [2112.12507].
- [53] C. Aimè et al., *Muon Collider Physics Summary*, in *2022 Snowmass Summer Study*, 3, 2022, 2203.07256.
- [54] M. Forslund and P. Meade, *High Precision Higgs from High Energy Muon Colliders*, 2203.09425.
- [55] J.-C. Yang, Z.-B. Qing, X.-Y. Han, Y.-C. Guo and T. Li, *Tri-photon at muon collider: a new process to probe the anomalous quartic gauge couplings*, *JHEP* **07** (2022) 053 [2204.08195].
- [56] J.-C. Yang, X.-Y. Han, Z.-B. Qin, T. Li and Y.-C. Guo, *Measuring the anomalous quartic gauge couplings in the  $W^+W^- \rightarrow W^+W^-$  process at muon collider using artificial neural networks*, *JHEP* **09** (2022) 074 [2204.10034].
- [57] A. Senol, S. Spor, E. Gurkanli, V. Cetinkaya, H. Denizli and M. Köksal, *Model-independent study on the anomalous  $ZZ\gamma$  and  $Z\gamma\gamma$  couplings at the future muon collider*, 2205.02912.
- [58] T. Li, H. Qin, C.-Y. Yao and M. Yuan, *Probing heavy triplet leptons of the type-III seesaw mechanism at future muon colliders*, *Phys. Rev. D* **106** (2022) 035021 [2205.04214].
- [59] S. Bottaro, D. Buttazzo, M. Costa, R. Franceschini, P. Panci, D. Redigolo et al., *The last Complex WIMPs standing*, 2205.04486.
- [60] I. Chakraborty, H. Roy and T. Srivastava, *Searches for heavy neutrinos at multi-TeV muon collider : a resonant leptogenesis perspective*, 2206.07037.
- [61] R. Capdevilla, D. Curtin, Y. Kahn and G. Krnjaic, *Discovering the physics of  $(g-2)_\mu$  at future muon colliders*, *Phys. Rev. D* **103** (2021) 075028 [2006.16277].
- [62] D. Buttazzo and P. Paradisi, *Probing the muon  $g-2$  anomaly with the Higgs boson at a muon collider*, *Phys. Rev. D* **104** (2021) 075021 [2012.02769].
- [63] W. Yin and M. Yamaguchi, *Muon  $g-2$  at multi-TeV muon collider*, 2012.03928.
- [64] G.-y. Huang, F. S. Queiroz and W. Rodejohann, *Gauged  $L_\mu-L_\tau$  at a muon collider*, *Phys. Rev. D* **103** (2021) 095005 [2101.04956].
- [65] R. Capdevilla, D. Curtin, Y. Kahn and G. Krnjaic, *No-lose theorem for discovering the new physics of  $(g-2)_\mu$  at muon colliders*, *Phys. Rev. D* **105** (2022) 015028 [2101.10334].
- [66] T. Li, M. A. Schmidt, C.-Y. Yao and M. Yuan, *Charged lepton flavor violation in light of the muon magnetic moment anomaly and colliders*, *Eur. Phys. J. C* **81** (2021) 811 [2104.04494].

- [67] G.-y. Huang, S. Jana, F. S. Queiroz and W. Rodejohann, *Probing the  $RK(*)$  anomaly at a muon collider*, *Phys. Rev. D* **105** (2022) 015013 [2103.01617].
- [68] P. Asadi, R. Capdevilla, C. Cesarotti and S. Homiller, *Searching for leptoquarks at future muon colliders*, *JHEP* **10** (2021) 182 [2104.05720].
- [69] S. Qian, C. Li, Q. Li, F. Meng, J. Xiao, T. Yang et al., *Searching for heavy leptoquarks at a muon collider*, *JHEP* **12** (2021) 047 [2109.01265].
- [70] W. Altmannshofer, S. A. Gadam and S. Profumo, *Snowmass White Paper: Probing New Physics with  $\mu^+\mu^- \rightarrow bs$  at a Muon Collider*, in *2022 Snowmass Summer Study*, 3, 2022, 2203.07495.
- [71] A. Azatov, F. Garosi, A. Greljo, D. Marzocca, J. Salko and S. Trifinopoulos, *New Physics in  $b \rightarrow s\mu\mu$ : FCC-hh or a Muon Collider?*, 2205.13552.
- [72] M. Battaglia, J.-J. Blaising, J. S. Marshall, S. Poss, A. Sailer, M. Thomson et al., *Physics performance for scalar electron, scalar muon and scalar neutrino searches at  $\sqrt{s} = 3$  TeV and 1.4 TeV at CLIC*, *JHEP* **09** (2013) 001 [1304.2825].
- [73] S. Homiller, Q. Lu and M. Reece, *Complementary Signals of Lepton Flavor Violation at a High-Energy Muon Collider*, in *2022 Snowmass Summer Study*, 3, 2022, 2203.08825.
- [74] A. Alvarez, R. Cepedello, M. Hirsch and W. Porod, *Temperature effects on the  $Z2$  symmetry breaking in the scotogenic model*, *Phys. Rev. D* **105** (2022) 035013 [2110.04311].
- [75] I. F. Ginzburg, K. A. Kanishev, M. Krawczyk and D. Sokolowska, *Evolution of Universe to the present inert phase*, *Phys. Rev. D* **82** (2010) 123533 [1009.4593].
- [76] G. C. Branco, P. M. Ferreira, L. Lavoura, M. N. Rebelo, M. Sher and J. P. Silva, *Theory and phenomenology of two-Higgs-doublet models*, *Phys. Rept.* **516** (2012) 1 [1106.0034].
- [77] R. Barbieri, L. J. Hall and V. S. Rychkov, *Improved naturalness with a heavy Higgs: An Alternative road to LHC physics*, *Phys. Rev. D* **74** (2006) 015007 [hep-ph/0603188].
- [78] J. A. Casas and A. Ibarra, *Oscillating neutrinos and  $\mu \rightarrow e, \gamma$* , *Nucl. Phys. B* **618** (2001) 171 [hep-ph/0103065].
- [79] P. F. de Salas, D. V. Forero, S. Gariazzo, P. Martínez-Miravé, O. Mena, C. A. Ternes et al., *2020 global reassessment of the neutrino oscillation picture*, *JHEP* **02** (2021) 071 [2006.11237].
- [80] MEG collaboration, A. M. Baldini et al., *Search for the lepton flavour violating decay  $\mu^+ \rightarrow e^+\gamma$  with the full dataset of the MEG experiment*, *Eur. Phys. J. C* **76** (2016) 434 [1605.05081].
- [81] BABAR collaboration, B. Aubert et al., *Searches for Lepton Flavor Violation in the Decays  $\tau_{+-} \rightarrow e^+ \gamma$  and  $\tau_{+-} \rightarrow \mu^+ \gamma$* , *Phys. Rev. Lett.* **104** (2010) 021802 [0908.2381].
- [82] SINDRUM collaboration, U. Bellgardt et al., *Search for the Decay  $\mu^+ \rightarrow e^+ e^+ e^-$* , *Nucl. Phys. B* **299** (1988) 1.

- [83] K. Hayasaka et al., *Search for Lepton Flavor Violating Tau Decays into Three Leptons with 719 Million Produced Tau+Tau- Pairs*, *Phys. Lett. B* **687** (2010) 139 [1001.3221].
- [84] S.-Y. Guo and Z.-L. Han, *Observable Signatures of Scotogenic Dirac Model*, *JHEP* **12** (2020) 062 [2005.08287].
- [85] SINDRUM II collaboration, C. Dohmen et al., *Test of lepton flavor conservation in  $\mu \rightarrow e$  conversion on titanium*, *Phys. Lett. B* **317** (1993) 631.
- [86] SINDRUM II collaboration, W. H. Bertl et al., *A Search for muon to electron conversion in muonic gold*, *Eur. Phys. J. C* **47** (2006) 337.
- [87] R. Kitano, M. Koike and Y. Okada, *Detailed calculation of lepton flavor violating muon electron conversion rate for various nuclei*, *Phys. Rev. D* **66** (2002) 096002 [hep-ph/0203110].
- [88] E. Arganda, M. J. Herrero and A. M. Teixeira,  *$\mu$ - $e$  conversion in nuclei within the CMSSM seesaw: Universality versus non-universality*, *JHEP* **10** (2007) 104 [0707.2955].
- [89] D. Borah and A. Dasgupta, *Common Origin of Neutrino Mass, Dark Matter and Dirac Leptogenesis*, *JCAP* **12** (2016) 034 [1608.03872].
- [90] ACME collaboration, J. Baron et al., *Order of Magnitude Smaller Limit on the Electric Dipole Moment of the Electron*, *Science* **343** (2014) 269 [1310.7534].
- [91] XENON collaboration, E. Aprile et al., *Dark Matter Search Results from a One Ton-Year Exposure of XENON1T*, *Phys. Rev. Lett.* **121** (2018) 111302 [1805.12562].
- [92] PANDAX-4T collaboration, Y. Meng et al., *Dark Matter Search Results from the PandaX-4T Commissioning Run*, *Phys. Rev. Lett.* **127** (2021) 261802 [2107.13438].
- [93] PLANCK collaboration, N. Aghanim et al., *Planck 2018 results. VI. Cosmological parameters*, *Astron. Astrophys.* **641** (2020) A6 [1807.06209].
- [94] A. Djouadi, M. Drees and J. L. Kneur, *Constraints on the minimal supergravity model and prospects for SUSY particle production at future linear  $e^+e^-$  colliders*, *JHEP* **08** (2001) 055 [hep-ph/0107316].
- [95] A. Costantini, F. De Lillo, F. Maltoni, L. Mantani, O. Mattelaer, R. Ruiz et al., *Vector boson fusion at multi-TeV muon colliders*, *JHEP* **09** (2020) 080 [2005.10289].
- [96] T. Han, Y. Ma and K. Xie, *High energy leptonic collisions and electroweak parton distribution functions*, *Phys. Rev. D* **103** (2021) L031301 [2007.14300].
- [97] R. Ruiz, A. Costantini, F. Maltoni and O. Mattelaer, *The Effective Vector Boson Approximation in high-energy muon collisions*, *JHEP* **06** (2022) 114 [2111.02442].
- [98] J. Alwall, R. Frederix, S. Frixione, V. Hirschi, F. Maltoni, O. Mattelaer et al., *The automated computation of tree-level and next-to-leading order differential cross sections, and their matching to parton shower simulations*, *JHEP* **07** (2014) 079 [1405.0301].
- [99] DELPHES 3 collaboration, J. de Favereau, C. Delaere, P. Demin, A. Giammanco,

- V. Lemaître, A. Mertens et al., *DELPHES 3, A modular framework for fast simulation of a generic collider experiment*, *JHEP* **02** (2014) 057 [[1307.6346](#)].
- [100] CMS collaboration, A. M. Sirunyan et al., *Performance of reconstruction and identification of  $\tau$  leptons decaying to hadrons and  $\nu_\tau$  in  $pp$  collisions at  $\sqrt{s} = 13$  TeV*, *JINST* **13** (2018) P10005 [[1809.02816](#)].
- [101] M. Casarsa, M. Fabbrichesi and E. Gabrielli, *Monochromatic single photon events at the muon collider*, *Phys. Rev. D* **105** (2022) 075008 [[2111.13220](#)].
- [102] M. Habermehl, M. Berggren and J. List, *WIMP Dark Matter at the International Linear Collider*, *Phys. Rev. D* **101** (2020) 075053 [[2001.03011](#)].
- [103] K. Black, T. Bose, Y. Chen, S. Dasu, H. Jia, D. Pinna et al., *Prospects for Heavy WIMP Dark Matter Searches at Muon Colliders*, in *2022 Snowmass Summer Study*, 5, 2022, [2205.10404](#).
- [104] J. L. Feng and D. E. Finnell, *Squark mass determination at the next generation of linear  $e^+e^-$  colliders*, *Phys. Rev. D* **49** (1994) 2369 [[hep-ph/9310211](#)].
- [105] C. G. Lester and D. J. Summers, *Measuring masses of semiinvisibly decaying particles pair produced at hadron colliders*, *Phys. Lett. B* **463** (1999) 99 [[hep-ph/9906349](#)].
- [106] C. G. Lester and B. Nachman, *Bisection-based asymmetric  $M_{T2}$  computation: a higher precision calculator than existing symmetric methods*, *JHEP* **03** (2015) 100 [[1411.4312](#)].